

## AFM-IR: Technology and Applications in Nanoscale Infrared Spectroscopy and Chemical Imaging

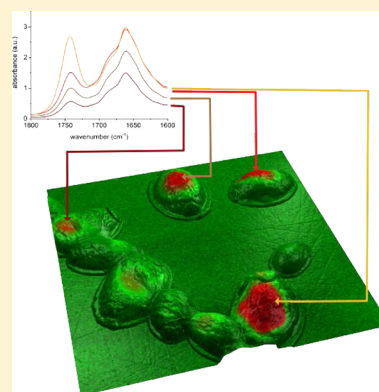
Alexandre Dazzi<sup>\*,†</sup> and Craig B. Prater<sup>‡</sup>

<sup>†</sup>Laboratoire de Chimie Physique, Univ. Paris-Sud, CNRS, Université Paris-Saclay, 91405 Orsay Cedex, France

<sup>‡</sup>Anasys Instruments, 325 Chapala St., Santa Barbara, California 93101, United States

### Supporting Information

**ABSTRACT:** Atomic force microscopy-based infrared spectroscopy (AFM-IR) is a rapidly emerging technique that provides chemical analysis and compositional mapping with spatial resolution far below conventional optical diffraction limits. AFM-IR works by using the tip of an AFM probe to locally detect thermal expansion in a sample resulting from absorption of infrared radiation. AFM-IR thus can provide the spatial resolution of AFM in combination with the chemical analysis and compositional imaging capabilities of infrared spectroscopy. This article briefly reviews the development and underlying technology of AFM-IR, including recent advances, and then surveys a wide range of applications and investigations using AFM-IR. AFM-IR applications that will be discussed include those in polymers, life sciences, photonics, solar cells, semiconductors, pharmaceuticals, and cultural heritage. In the [Supporting Information](#), the authors provide a theoretical section that reviews the physics underlying the AFM-IR measurement and detection mechanisms.



### CONTENTS

1. Introduction	5146	3.3.2. Photonics and Plasmonics	5165
2. AFM-IR Technology overview	5147	3.3.3. AFM-IR in Semiconductors	5167
2.1. History of AFM-IR Development	5148	3.3.4. AFM-IR in Cultural Heritage	5168
2.2. Details of AFM-IR Operation	5148	4. Conclusion	5169
2.3. Complementary Nanomechanical Measurements via Contact Resonance	5149	Associated Content	5169
2.4. Resonance-Enhanced AFM-IR	5150	Supporting Information	5169
2.5. Other Recent Advances in AFM-IR	5150	Author Information	5170
2.6. Comparison with Related Techniques	5150	Corresponding Author	5170
3. AFM-IR Applications	5151	Notes	5170
3.1. AFM-IR of Polymers	5151	Biographies	5170
3.1.1. Polymer Blends and Composites	5151	Acknowledgments	5170
3.1.2. Quantification of Chemical Content	5152	References	5170
3.1.3. AFM-IR of Polymer Multilayer Films	5153		
3.1.4. AFM-IR Applications in Polymeric Fibers	5153		
3.1.5. AFM-IR of Conducting Polymer Materials	5156		
3.1.6. AFM-IR Applications in Medical Devices/Failure Analysis	5156		
3.1.7. Coatings	5157		
3.2. AFM-IR Applications in Life Sciences	5157		
3.2.1. Biodiesel Production	5157		
3.2.2. Single Cells and Infrared Tags	5159		
3.2.3. Tissue	5162		
3.2.4. Protein Aggregation and Secondary Structure	5163		
3.2.5. AFM-IR in Pharmaceutical Sciences	5164		
3.3. Other Applications of AFM-IR	5165		
3.3.1. Perovskite Solar Cells	5165		

### 1. INTRODUCTION

AFM-based infrared spectroscopy (AFM-IR)<sup>1–4</sup> is a hybrid technique that combines the spatial resolution of atomic force microscopy (AFM) with the chemical analysis capability of infrared (IR) spectroscopy. Individually AFM and infrared spectroscopy are powerful and widely used techniques. AFM is routinely used for topographic imaging of diverse samples in materials and life science research as well as many industrial applications. Infrared spectroscopy is one of the most widely used techniques for chemical analysis. Infrared spectroscopy performs chemical characterization by measuring infrared absorption spectra [i.e., the amount of infrared light absorbed

**Special Issue:** Vibrational Nanoscopy

**Received:** July 11, 2016

**Published:** December 13, 2016

by a sample as a function of the frequency (or equivalently wavelength) of the IR light]. The pattern of absorption peaks in the IR spectra serve as a fingerprint that can be used to characterize and/or identify chemical species. In the mid 1990's, infrared spectroscopy was also combined with microscopy and array detectors to enable spatially resolved infrared microspectroscopy. This technique has also been extremely successful in providing imaging based on chemical contrast as well as the ability to chemically analyze microscopic regions of a sample. Two prior reviews have been written on the subject, one focused on the AFM-IR technique<sup>4</sup> and another that places it in context with scattering-based scanning near-field optical microscopy.<sup>5</sup>

AFM-IR was developed to overcome two major limitations of the predecessor technologies of AFM and infrared microspectroscopy. Conventional infrared spectroscopy based on FT-IR-based microscopes has been widely used for spatially resolved chemical analysis. The main drawbacks of infrared microspectroscopy have been performance limits due to low brilliance of thermal IR sources and spatial resolution limit set by optical diffraction. Optical diffraction typically sets a fundamental limit for spatial resolution of  $\lambda/2$ , where  $\lambda$  is the illuminating wavelength. Most commercial FT-IR microscopes based on a thermal IR source have had a practical spatial resolution limited to  $\lambda$  to  $3\lambda$ , thus achieving spatial resolution in the range of 2.5–75  $\mu\text{m}$ , depending on the specific technique and configuration employed.<sup>6,7</sup> FT-IR microscopes have been coupled to high-brilliance synchrotron IR beamlines,<sup>8</sup> where diffraction limited performance has been achieved. Recent improved in optics and array detectors have demonstrated the ability of FT-IR microscopy to achieve spatial resolution approaching 1  $\mu\text{m}$  scale even with a thermal source,<sup>9,10</sup> but most conventional infrared microspectroscopy applications have been constrained to research and industrial characterization problems on the length scale of many micrometers and above.

Atomic force microscopy, on the other hand, can routinely achieve spatial resolution on the nanometer scale. AFM has a spatial resolution limited only by the radius of the apex of the AFM probe tip. Commercially available AFM tips routinely achieve spatial resolution on length scales <20 nm and in some cases down to the molecular and atomic scale. The AFM however does not have any intrinsic ability to discriminate materials on the basis of chemical composition. A large number of AFM-based techniques<sup>11–17</sup> have been developed over the years to discriminate materials on the basis of various material properties like friction/adhesion, elasticity, damping, optical, electronic and magnetic properties, for example. But none of these techniques provided a broadly applicable method of performing unambiguous chemical analysis. For this reason, the developers of the AFM-IR technique were highly motivated to develop a technique to provide the chemical analysis capabilities of infrared spectroscopy with the spatial resolution of the AFM. AFM-IR achieves this goal by using the tip of an atomic force microscope to locally detect thermal expansion of a sample resulting from local absorption of IR radiation. The AFM tip itself thus acts as the IR detector. Because the AFM tip can detect the thermal expansion with spatial resolution approaching the AFM tip radius, the AFM-IR technique can overcome the spatial resolution limits of conventional IR microspectroscopy.

This article reviews AFM-IR technology and applications and underlying theory in the [Supporting Information](#). The next

section includes a brief history of the development of AFM-IR and a detailed explanation of its operation. In [section 3](#), we survey a diverse range of AFM-IR applications, including those in materials and life sciences. We dedicate a significant discussion to applications in polymers sciences and technology, including applications on polymer blends, composites, multi-layer films, fibers, and conducting polymers. AFM-IR is also finding exciting applications in the life sciences, including subcellular spectroscopy and chemical imaging, nanoscale chemical analysis of tissue, protein secondary structure analysis, including research into protein misfolding related neurodegenerative diseases. We also survey additional applications including photonics, pharmaceutical sciences, perovskites (solar energy), and semiconductors.

Finally, in the [Supporting Information](#), we discuss a mathematical theory that underlies the operation of the AFM-IR technique.

## 2. AFM-IR TECHNOLOGY OVERVIEW

In its current form ([Figure 1](#)), AFM-IR consists of a tunable infrared laser that is focused onto a region of a sample in the

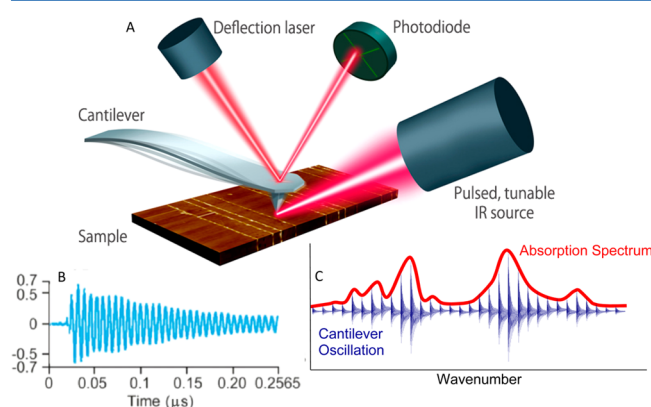


**Figure 1.** (A) Schematic diagram of AFM-IR. A pulsed tunable laser source is focused on a sample near the tip of an atomic force microscope. When the laser is tuned to an absorbing band of the sample, the absorbed light results in photothermal expansion of absorbing regions of the sample. The AFM tip is used as a local detector of IR absorption. (B) The sample's photothermal expansion induces a transient cantilever oscillation that is proportional to the IR absorption. (C) Measuring the AFM cantilever oscillation amplitude as a function of wavelength (or wavenumber) results in a local absorption spectrum with nanoscale spatial resolution. Image courtesy of Anasys Instruments, reprinted with permission.

proximity of a probe tip from an atomic force microscope. If the tunable IR laser is set to a wavelength that corresponds to an absorbing wavelength of the sample, the AFM tip can be used to detect the absorbed radiation. The most common technique to detect the IR absorption is by a direct measurement of the thermal expansion resulting from optical absorption. The IR absorption causes a force impulse on the tip of the cantilever, inducing an oscillation of the AFM cantilever probe. As discussed below, it is also possible to measure the sample temperature increase due to absorbed IR radiation as an alternative to measuring the cantilever motion. By measuring the AFM probe response to IR absorption as a function of wavelength, it is possible to readily create IR absorption spectra of nanoscale regions of a sample. Additionally, it is possible to tune the laser to a fixed wavelength and measure the absorption



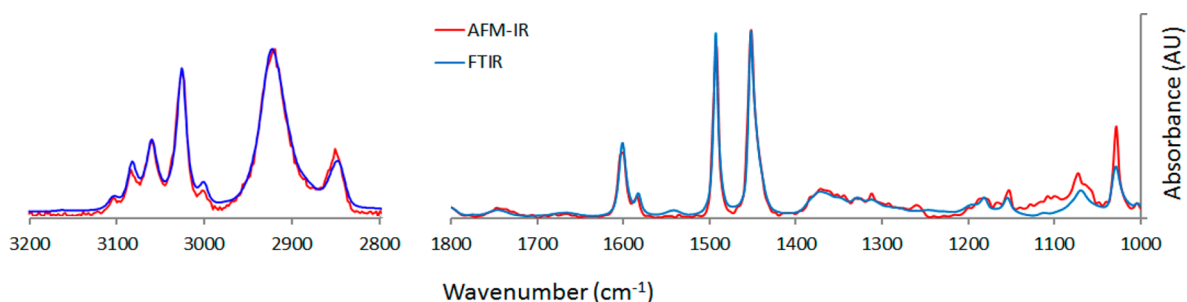


**Figure 2.** Comparison of AFM-IR and bulk FT-IR spectra on polystyrene. Because the AFM-IR cantilever oscillation amplitude is linearly dependent on the IR absorption coefficient,<sup>33,34</sup> AFM-IR correlate very well to bulk IR transmission spectra.<sup>4</sup> Reprinted with permission. Copyright 2012 Anasys Instruments.

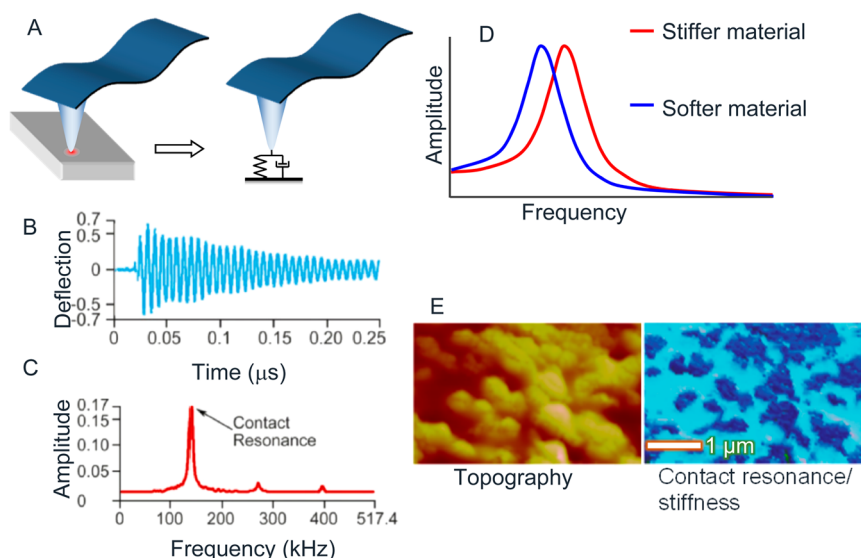


**Figure 3.** AFM-IR provides complementary measurements of nanomechanical properties of the sample. (A) The tip–sample contact region acts like a spring–damper system that affects the contact resonance frequencies of the AFM cantilever probe. (B) When the sample absorbs IR radiation, the resulting thermal expansion causes the AFM cantilever to oscillate. (C) By taking the FFT of the cantilever oscillation signal, it is possible to extract the contact resonance frequencies of the cantilever. (D) These resonant frequencies shift as a function of the stiffness of the sample. (E) Mapping the contact resonance frequency as a function of position allows mapping of the sample stiffness. The contact resonance/stiffness measurements can be obtained simultaneously with AFM-IR measurements, enabling correlative measurements of mechanical properties and chemical composition. Adapted with permission from ref 4. Copyright 2012 OSA Publishing.

as a function of position across the sample to create chemical images that show the distribution of chemical species across a sample.

### 2.1. History of AFM-IR Development

The first work combining AFM and infrared spectroscopy was performed separately but at roughly the same time by Hammiche<sup>18</sup> et al. in the UK and Anderson<sup>19</sup> at the Jet Propulsion Laboratory in the U.S. Both researchers used a commercial Fourier Transform Infrared (FT-IR) spectrometer as the infrared source and coupled this beam to the tip and sample of an atomic force microscope. Hammiche and his collaborators used temperature-sensing Wollaston wire probes to detect the heat resulting from IR absorption.<sup>18</sup> Anderson chopped the IR beam at low frequencies and measured the change in the deflection of the AFM cantilever due to thermal expansion of the sample.<sup>19</sup> The current AFM-IR technique at the focus of this review article was developed by Dazzi et al.<sup>1–4</sup> who used a tunable free electron laser source to excite resonant oscillations in an AFM probe due to absorption of IR radiation pulses by the sample. This combination for the first time provided the ability to perform both broadband point

spectroscopy and the ability to do rapid narrow band chemical composition mapping. Commercial instruments were first developed by Anasys Instruments and collaborators using a broadly tunable parametric oscillator (OPO)<sup>20,21</sup> laser source with nanosecond pulses. Belkin et al.<sup>22,23</sup> demonstrated the use of photothermal AFM-IR with tunable quantum cascade based laser sources, enabling dramatic improvements in sensitivity, as will be discussed below. The photothermal technique employed in AFM-IR has also been used to detect absorption of visible light<sup>24</sup> and is sometimes referred to as Photothermal Induced Resonance (PTIR) as it is not constrained solely to infrared wavelengths.

### 2.2. Details of AFM-IR Operation

As mentioned above and illustrated in Figure 1, AFM-IR works by detecting light absorbed by the sample. The absorbed light generates a temperature increase that can be detected directly with a temperature sensing probe, or more commonly by a transient force induced on the tip of an AFM in contact with the absorbing region of the sample surface. When light is absorbed by the sample, the resulting temperature increase causes an almost instantaneous thermal expansion of the

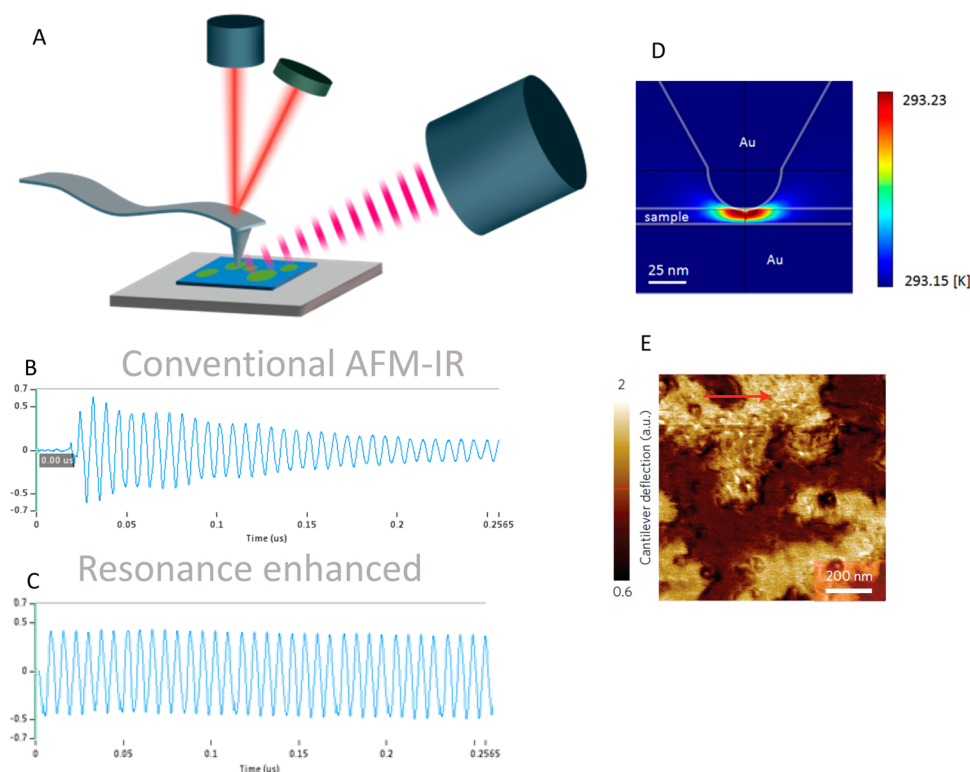


**Figure 4.** (A) Resonance-enhanced AFM-IR<sup>22,23</sup> improves the sensitivity versus conventional AFM-IR by pulsing the laser at a contact resonance frequency of the AFM cantilever. (B) While conventional AFM-IR results in a transient decaying oscillation of the cantilever, (C) resonance-enhanced AFM-IR results in a continuous wave oscillation of the cantilever. (D) Combined with “lightning rod” enhancement from metallic tips and/or substrates, resonance-enhanced AFM-IR results in significant sensitivity improvements that have enabled the successful measurement AFM-IR spectra and IR absorbance images on very thin samples, including self-assembled monolayers (E, adapted with permission from ref 23. Copyright 2014 Nature Publishing Group).

sample. This thermal expansion increases until the light pulse ends and then the sample temperature exponentially decays back toward the ambient temperature at a rate dependent on the thermal properties of the sample. (This will be discussed in more detail in the [Supporting Information](#) on AFM-IR theory.) This thermal expansion acts as a force impulse on the cantilever that drives the cantilever into oscillation. Because of the typical short duration of the force impulse, the cantilever is driven into oscillation over multiple oscillatory modes (eigenmodes) of the cantilever. When operated in contact mode AFM, the eigenmodes of the cantilever correspond to contact resonances,<sup>25–32</sup> the frequency of which can also provide complementary information about the mechanical stiffness of the sample.<sup>4</sup> For most cases, the oscillation amplitude of the cantilever is directly proportional to the amount of light absorbed and this in turn is directly proportional to the absorption coefficient.<sup>33,34</sup> Although the AFM-IR signal strength does depend on other material properties of the sample (e.g., sample thermal expansion coefficient, heat capacity, density, and modulus), these properties remain constant at a specific point on the sample. As such, measuring the oscillation amplitude of the cantilever at a fixed point on a sample as a function of wavelength (or equivalently, wave-number) provides a signal that is directly proportional to the absorption coefficient. For this reason it is possible to obtain IR absorption spectra that correlate to bulk transmission infrared spectroscopy (e.g., FT-IR) because the AFM-IR technique in effect measures the same physical property (i.e., the amount of absorbed light) (Figure 2).

AFM-IR measurements are typically performed by measuring the oscillation amplitude of the cantilever as a function of wavelength (in the case of spectroscopy) or sample position (for chemical imaging). Measurements are performed by either measuring the peak-to-peak oscillation amplitude of the cantilever or the oscillation amplitude at any specific oscillation mode (eigenmode) of the cantilever. In some cases, higher-order modes are employed to improve the signal-to-noise ratio and/or improve the rejection of nonlocal background forces that can result from the heating of the air near the cantilever.

### 2.3. Complementary Nanomechanical Measurements via Contact Resonance

The AFM-IR technique can also provide simultaneous and complementary measurements of the mechanical properties of the sample with nanometer-scale spatial resolution. As mentioned previously, when the cantilever is excited by the sample thermal expansion due to absorption of IR radiation, the force impulse drives the cantilever into oscillation at contact resonance frequencies of the cantilever. The peak frequencies of these contact resonances can shift depending on the stiffness of the sample. As illustrated in Figure 3, the tip–sample contact acts like a spring-damper system that is coupled to the tip of the AFM. As the elasticity and/or damping of the sample changes, the contact resonance frequencies and quality factors of the resonance also change. The contact resonance frequency can be measured synchronously with the AFM-IR absorption measurement by simply performing a fast Fourier transform (FFT) on the cantilever ringdown.

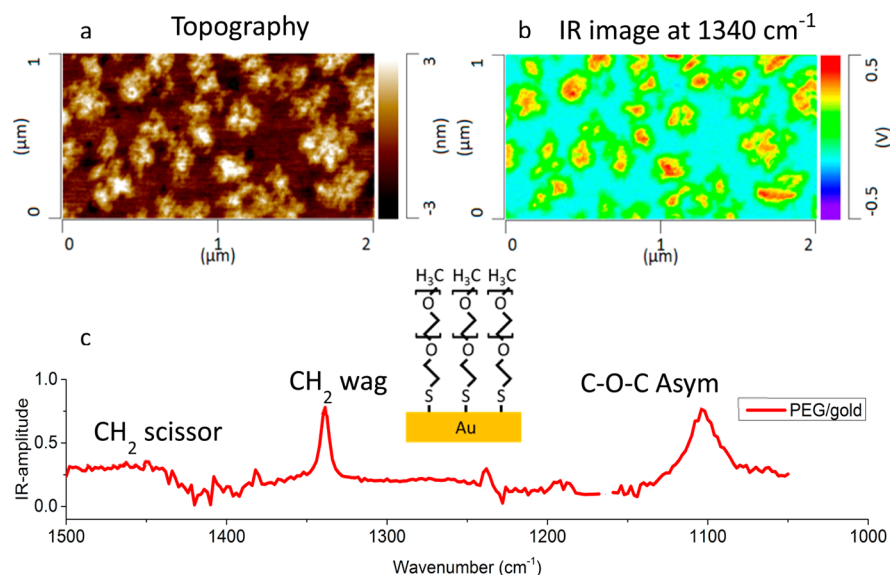


**Figure 5.** Resonance-enhanced AFM-IR of a self-assembled monolayer of PEG on gold. (a) AFM topographic image. (b) AFM-IR absorption image at  $1340\text{ cm}^{-1}$ , corresponding to the  $\text{CH}_2$  wag as shown in the (c) AFM-IR spectrum of the monolayer. Sample courtesy of M. Belkin, University of Texas. Image reprinted with permission. Copyright 2014 Anasys Instruments.

## 2.4. Resonance-Enhanced AFM-IR

The original operation of AFM-IR worked with relatively low repetition rate IR sources (e.g., a few Hz with the free electron laser used by Dazzi et al.<sup>1,12</sup> and 1 kHz used in the optical parametric oscillator (OPO) in the AFM-IR system originally commercialized by Anasys Instruments). Lu et al. in Mikhail Belkin's group at the University of Texas demonstrated significant improvements in the sensitivity of AFM-IR using a much higher repetition rate laser source based on a quantum cascade laser (QCL).<sup>22,23</sup> In fact, Lu et al. tuned the repetition rate of the QCL to match one of the contact mode resonances of the AFM cantilever, as discussed above. In this mode of operation, the cantilever oscillation changes from a decaying transient oscillation into a continuous wave oscillation as shown in Figure 4. This so-called "resonance enhanced AFM-IR" provides a continuous wave oscillation of the cantilever that allows for much more efficient detection of the IR absorption and thus more sensitive measurements. The Belkin group also demonstrated the ability to further enhance the sensitivity of AFM-IR using metal-coated AFM tips and optionally metal-coated sample substrates. With metal-coated tips (and substrates), the local electric field generated by the incident radiation is focused and intensified at the apex of the AFM tip. Coupling the so-called "lightning rod effect" with resonance-enhanced AFM-IR has enabled nanoscale IR spectroscopy and chemical imaging on samples as thin as  $\sim 5\text{ nm}$  biological membranes and even single self-assembled monolayers.<sup>23</sup>

Figure 5 shows the AFM topography image (top left) and an IR absorption image with the QCL tuned to the fixed wavenumber of  $1340\text{ cm}^{-1}$  (top right) of a monolayer island film of an alkyl thiol ethoxylate (PEG) self-assembled onto a template-stripped gold substrate. The AFM topography image suggests the PEG islands are about  $5\text{ nm}$  thick. The IR absorption band at  $1340\text{ cm}^{-1}$  is assigned to a  $\text{CH}_2$ -wagging mode, and the image confirms the location of the PEG island regions. PEG monolayer island regions as small as  $25 \times 25\text{ nm}$  are easily resolved in the IR absorption image. The AFM-IR spectrum of one of the PEG islands is shown at the bottom of Figure 5. The broad IR band centered at  $1102\text{ cm}^{-1}$  is assigned

to the C–O–C antisymmetric stretching mode. The absence of an expected  $\text{CH}_2$  scissoring vibrational absorbance near  $1465\text{ cm}^{-1}$  suggests that the PEG chains are oriented normal to the gold substrate surface.

## 2.5. Other Recent Advances in AFM-IR

Other recent advances in AFM-IR have demonstrated improvements in spectral range, sensitivity, and other figures of merit. Research at NIST used a picosecond laser source and extended the spectral range to both longer mid-IR wavelengths<sup>35</sup> and also even into the visible.<sup>24</sup> Cho et al. demonstrated improvements in signal-to-noise using frequency and temporal filtering techniques.<sup>36</sup> The NIST group also investigated the use of high-resolution and high-frequency temperature sensing probes to directly measure the local heating rather than the local thermal expansion.<sup>37</sup>

## 2.6. Comparison with Related Techniques

AFM-IR has important differences from other complementary techniques that have been used to perform nanoscale spectroscopy and subwavelength infrared imaging, most notably scattering scanning near field optical microscopy (s-SNOM)<sup>38</sup> and tip-enhanced Raman spectroscopy (TERS).<sup>39–41</sup> A complete review of these subjects is outside the scope of this article, and the reader is referred to recent reviews on s-SNOM<sup>5,42</sup> and TERS<sup>43–45</sup> for more information, but we shall briefly contrast AFM-IR versus these other techniques. The most significant difference between AFM-IR and s-SNOM/TERS is that AFM-IR measures light absorbed by the sample, whereas s-SNOM and TERS both measure light scattered by the sample. As such, the s-SNOM and TERS techniques perform best where the samples are strong scatterers of light. For the TERS technique, this can be a particular challenge as Raman scattering has a much lower cross section than elastically scattered light used in s-SNOM. To detect Raman scattered light with sufficient sensitivity, the TERS technique employs special field-enhancing tips to (ideally) dramatically enhance the amount of Raman shifted light that is scattered from a small region around the probe tip. A key limitation of the TERS technique has been related to



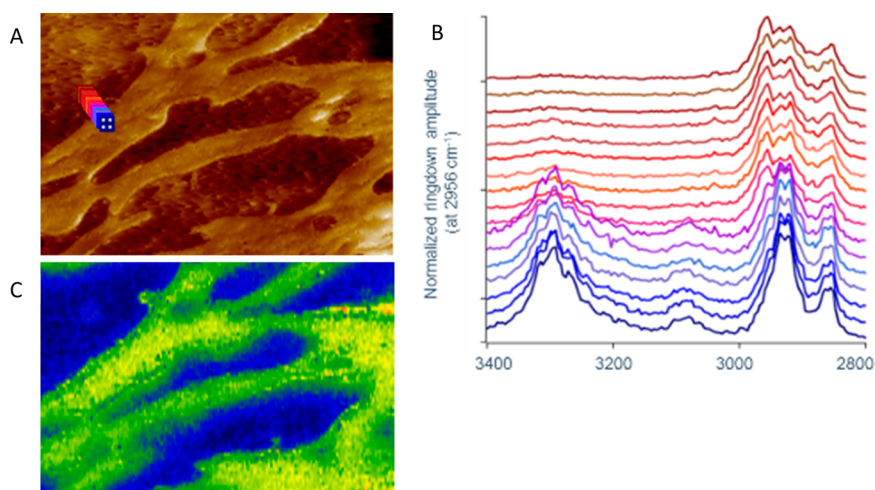


**Figure 6.** AFM-IR measurements of a blend of nylon and natural rubber. (A) AFM image and (B) AFM-IR absorption spectra obtained at locations indicated in (A). The AFM-IR spectra across the boundary shows the clear appearance of the NH-stretching band associated with the nylon as well as other more subtle changes. (C) Chemical map of the nylon/rubber blend. This image was obtained by constructing a ratio of IR absorption images at  $3300\text{ cm}^{-1}/2956\text{ cm}^{-1}$ , where  $3300\text{ cm}^{-1}$  corresponds to the NH-stretching absorption from the nylon versus the  $\text{CH}_3$  antisymmetric stretching band at  $2956\text{ cm}^{-1}$ , which occurs more distinctly in the natural rubber component of the blend. In this ratio image, the nylon regions are blue and the natural rubber appears yellow-green. Reprinted with permission. Copyright 2013 Anasys Instruments.

manufacture of field enhancing probe tips with a sufficiently large and reproducible enhancement factors, especially in commercially available probes. AFM-IR, by contrast, uses readily available commercial AFM probes without the need for large enhancement factors. In comparing AFM-IR and s-SNOM, it is instructive to consider the mechanism of the detection methods. AFM-IR provides a direct measurement of the absorption of light via detection as the detected signal is directly proportional to the sample's absorption coefficient.<sup>33,34</sup> In contrast, the s-SNOM technique measures the amount of light scattered from the sample, which in turn can depend on the complex optical properties of the tip, sample and underlying substrate. It is possible, though not trivial, in the s-SNOM technique to approximate the complex optical properties of the sample by using interferometric detection techniques along with careful modeling of the radiation/tip/sample interactions.<sup>46</sup> Due to the complex dependence on sample and substrate properties, the s-SNOM technique is susceptible to sample thickness and substrate induced shifts in the position of absorption peaks.<sup>47</sup> AFM-IR measurements can be performed without the complexity of interferometric detection, and absorption spectra can be obtained directly without modeling, with absorption peaks correlating well to FT-IR and without thickness-dependent peak shifts. Another key difference is that s-SNOM and TERS techniques are primarily surface sensitive, whereas AFM-IR can be sensitive to the absorption of IR radiation to a greater depth into the sample.

### 3. AFM-IR APPLICATIONS

#### 3.1. AFM-IR of Polymers

AFM-IR is finding numerous applications in the field of polymers both in academia and industry.<sup>4</sup> Specific applications have included biodegradable polymers,<sup>48</sup> polymer blends,<sup>49,50</sup> and composites,<sup>51</sup> multilayer films,<sup>52</sup> polymer nanostructures,<sup>53,54</sup> thin films/coatings, fibers,<sup>55</sup> fuel cell membranes,<sup>56</sup> biomedical materials, and pharmaceuticals.<sup>57–61</sup> In each of these areas, polymer performance demands are driving formulations and structures with micro- and nanoscale feature

sizes. Conventional IR microspectroscopy has not been able to provide the spatial resolution required to keep up with the analytical characterization needs of these materials. AFM-IR has provided the ability to measure and map chemical content in nanoscaled polymer domains, identify and characterize extremely thin layers in laminated polymer multilayer films, map and analyze films, even down to monolayer coverage, and track degradation in biomedical materials. This section will highlight some of these applications in more detail.

**3.1.1. Polymer Blends and Composites.** Polymer blends and polymer nanocomposites are a keen area of interest in academic and industrial R&D. Performance polymer systems are expected to be a \$20B industry by 2020. As distinguished from commodity polymers, performance polymers attempt to achieve superior performance in aspects like strength, toughness, weight, specific electrical or thermal properties, resistance to degradation, or other properties. To achieve this target performance, engineering polymers are often complex formulations of multiple polymeric components, additives, fillers, compatibilizers, etc., often with material heterogeneity on the micro- and nanoscales. The AFM-IR is providing critical insights into the distribution of the different polymer components, how they segregate, and how they interface. It is also possible to use the AFM-IR system to map the distribution of different chemical components. Since AFM-IR uses narrowband tunable IR sources, it is possible to tune the laser to any specific absorption band and then map the intensity of the IR absorption as a function of position on the sample surface. Figure 6 shows an example of AFM-IR spectra and absorption mapping on a polymer blend of nylon and natural rubber. A series of spectra were first obtained across an interface between the two materials. From the spectra, it was possible to identify key IR absorption bands that were characteristic with the constituent components. By creating a ratiometric image of IR absorptions at the different selected bands, it is possible to unambiguously map the distribution of the different chemical components.

Marcott et al. have used AFM-IR to study degradable polymer materials, including observing local variations in

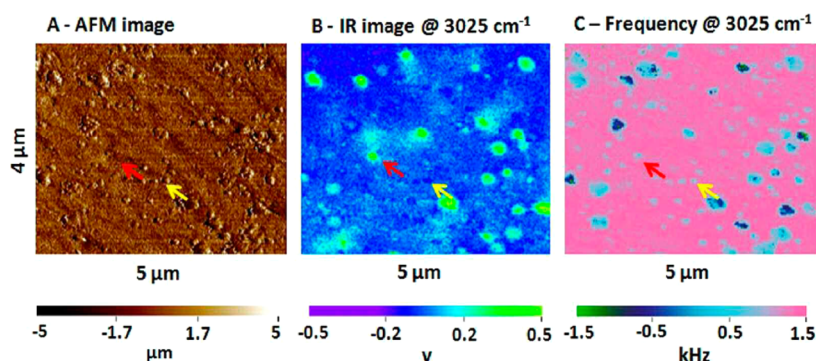


**Figure 7.** AFM-IR measurements of a 100% ABS polymer sample. (A) AFM topographic image. (B) AFM-IR absorption map with the IR source tuned to  $3025\text{ cm}^{-1}$ , corresponding to a strong styrene absorption. (C) A simultaneously obtained contact resonance frequency image that is indicative of the relative sample stiffness. Red arrows point to regions of high PS concentration. The yellow arrows indicate softer regions corresponding to higher PB content. Reprinted with permission from ref 49. Copyright 2012 John Wiley and Sons.

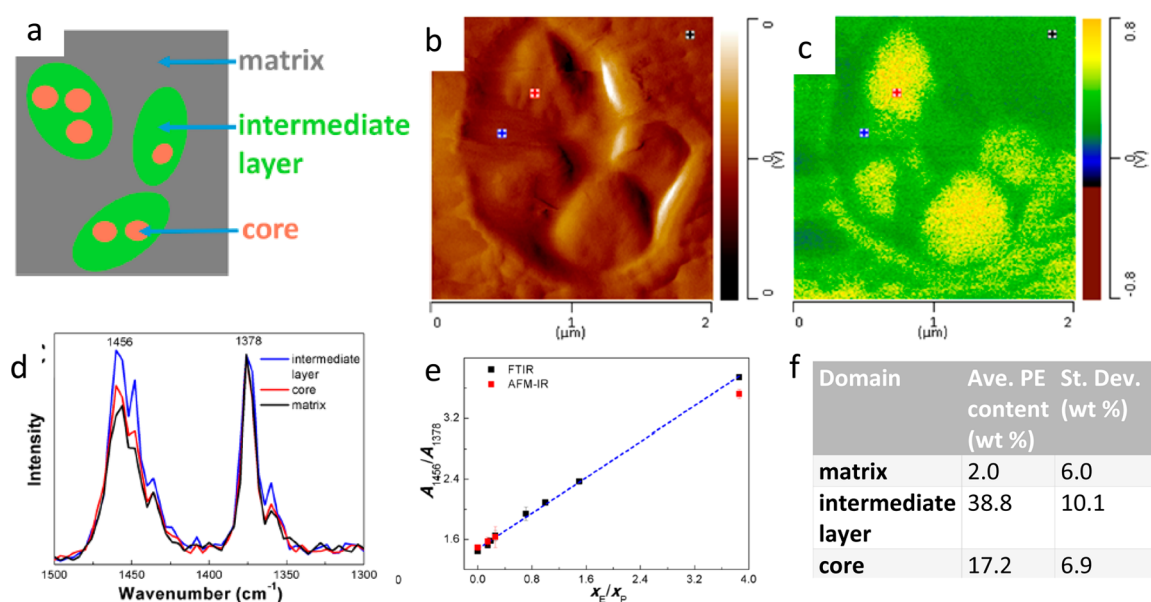


**Figure 8.** AFM-IR measurements of a high impact polypropylene (HIPP) polymer blend demonstrating the ability to quantify chemical composition within nanoscale domains. (a) Schematic structure of the HIPS material. (b) AFM image of an intermediate layer region within the matrix. (c) AFM-IR image obtained at  $1378\text{ cm}^{-1}$ . (d) AFM-IR spectra obtained at different regions on the sample corresponding to matrix, intermediate layer, and core. (e) Calibration curve based on bulk FT-IR that links the concentration of PE within the material to the ratio of the peak intensity of the  $1456$  and  $1378\text{ cm}^{-1}$  absorption bands. (f) Estimates of the percentage PE concentration in the different regions illustrated in (a). Adapted from ref 50. Copyright 2016 American Chemical Society.

crystallinity on the nanoscale, as well as observing effects associated with annealing.<sup>48</sup> Ye et al. performed AFM-IR measurements of blends of acrylonitrile butadiene styrene (ABS) thermoplastic polymer (ABS) with varying concentrations of polycarbonate (PC).<sup>49</sup> ABS is known to phase segregate into domains rich in polybutadiene (PB) and regions rich in polystyrene (PS). Figure 7 shows AFM-IR measurements that demonstrate the ability to discriminate the phase-segregated domains both on the basis of IR absorption (using a characteristic absorption of the PS) and stiffness based on the elasticity difference between the PB and PS domains.

**3.1.2. Quantification of Chemical Content.** Recent research by Tang et al. has also demonstrated the ability to quantify the concentration of polymeric components in nanoscale domains of complex polymer blends.<sup>50</sup> The researchers used AFM-IR to study polymeric component distribution in high impact polypropylene (HIPP). By using a concentration calibration performed with conventional FT-IR,

Tang et al. was able to use relative absorption peak heights to quantitatively estimate the percentage of polymeric components in different regions of HIPP samples, including the distribution of components in nanoscale domains. Figure 8 illustrates the approach used by Tang et al. to achieve this quantification of chemical content.

AFM-IR has also been used to study a variety of nanocomposite materials. A recent study by Brown and Bhusan<sup>51</sup> investigated nanocomposite materials being studied for oil-repellent films. The nanocomposites comprised polycarbonate treated with an acetone–nanoparticle mixture. Agglomeration of nanoparticles created re-entrant structures intended to create surfaces resistant to oil. AFM-IR was used to study the distribution of polycarbonate and assess the crystallization in the vicinity of the nanoparticle (Figure 9). The results indicate that the PC is more crystalline when near the nanoparticle.

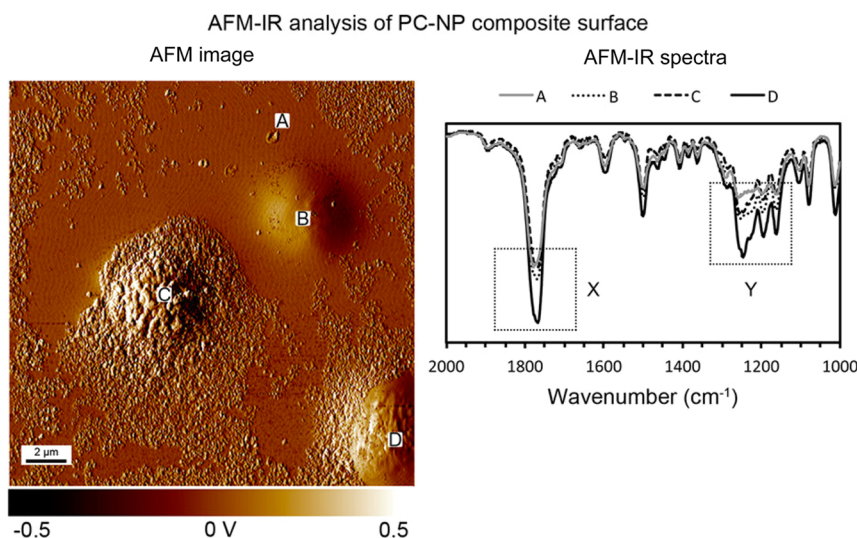


**Figure 9.** AFM-IR spectroscopic analysis of a polymer nanocomposite involving re-entrant hierarchical structures. The AFM-IR analysis examined the distribution of polycarbonate and polymer crystallinity relative to the re-entrant structures. Adapted with permission from ref [51](#) under Creative Commons license. Copyright 2016 Nature Publishing Group.

**3.1.3. AFM-IR of Polymer Multilayer Films.** Similarly, multilayer laminated films which are used extensively in a multitude of applications, including in packaging of food, drugs, consumer products, stretch films, electronics and displays, and other areas. Multilayer polymer films can consist of many layers, and these layers increasingly involve submicron or even nanometer scale dimensions that are below the resolution limits of convention IR microspectroscopy. Multilayer films also usually consist of different polymer layers with distinct properties chosen, for example, for structural integrity, barrier properties, printability, specific optical, or electronic properties, etc. Many of these dissimilar materials may lack binding affinity to adjacent layers and as such materials called compatibilizers are often used at the interface between layers to provide adhesion. AFM-IR has been used in a variety of applications in the field of multilayer films, including measuring the thickness and uniformity of polymer layers, characterizing the interface between layers, and even identifying unknown materials in competitive products (e.g., reverse engineering).

One of the key concerns in the manufacturing of multilayer films is the uniformity of the films. By tuning the AFM-IR laser to an absorption band of one of the layer components, variations in uniformity are easily revealed, even for submicron layers. [Figure 10](#) shows an example of AFM-IR measurements of a multilayer polymer film with alternating layers of  $\sim 200$  nm and  $\sim 20$  nm thickness.

AFM-IR has also been used extensively to study the chemical composition of multilayer films,<sup>62</sup> including to reverse engineer their composition<sup>52</sup> and to study interfaces between layers. Eby et al. examined a multilayer film of originally unknown composition via AFM-IR and were able to determine the composition of each layer by comparing AFM-IR spectra to FT-IR reference spectra.<sup>52</sup> From the AFM-IR spectra shown in [Figure 11](#), it is clear that layers 1 and 2 contain poly(ethyleneterephthalate) (PET), while layer 3 is a poly(urethane). The inclusions in layer 4 are clearly visible, and AFM-IR spectra at several locations are displaying broad absorptions around  $3330\text{ cm}^{-1}$  and at  $1640\text{ cm}^{-1}$ . In addition, antisymmetric and symmetric  $\text{CH}_2$ -stretching bands are strong and sharp; a methyl  $\text{CH}$ -stretching band is also observed at

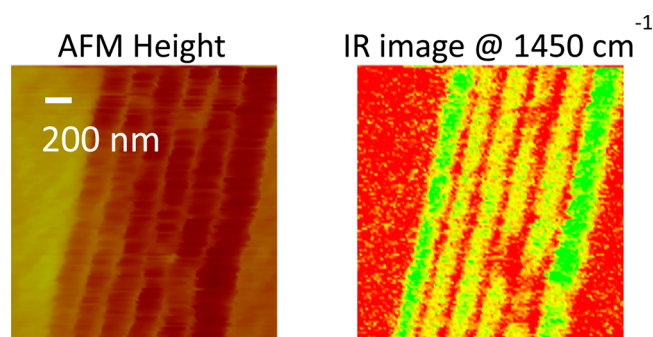


**Figure 10.** AFM (left) and AFM-IR absorption image (right) of a multilayer laminate film. The AFM-IR absorption image clearly reveals nonuniformity in the layers as well as localized defects. Reprinted with permission. Copyright 2014 Anasys Instruments.

$2952\text{ cm}^{-1}$ . However, the IR absorption spectrum of the  $1.2\text{ }\mu\text{m}$  inclusion lacks these strong bands (not shown). These data suggest the core component of layer 4 is polyethylene, and the inclusions are hydroxyl-containing materials such as starch or cellulose.

**3.1.4. AFM-IR Applications in Polymeric Fibers.** AFM-IR has also been applied to the study of a variety of applications in fibers, including textile fibers, natural fibers, fiber-epoxy composites, highly oriented polymer fibers, and nanofibers. The following sections review a few examples.

**3.1.4.1. Electrospun Nanofibers.** Currently, there is considerable research in the area of electrospun nanofibers. These fibers that are manufactured via a solvent/polymer mixture being ejected from a syringe under high voltage. The manufacturing process can lead to nanoscale fibers with a high degree of uniformity and molecular orientation. Electrospun fibers hold promise for applications in a broad range of fields, including drug delivery, tissue engineering, wound dressing and cosmetics, functional materials and devices such as composite reinforcement, filters, protective clothing, and smart textiles, electronics, sensors, and catalysts.<sup>63</sup> AFM-IR has recently been used to study the molecular conformation and molecular orientation electrospun nanofibers.<sup>4,55</sup> In recent work by Gong et al.<sup>55</sup> at the University of Delaware, AFM-IR was used to



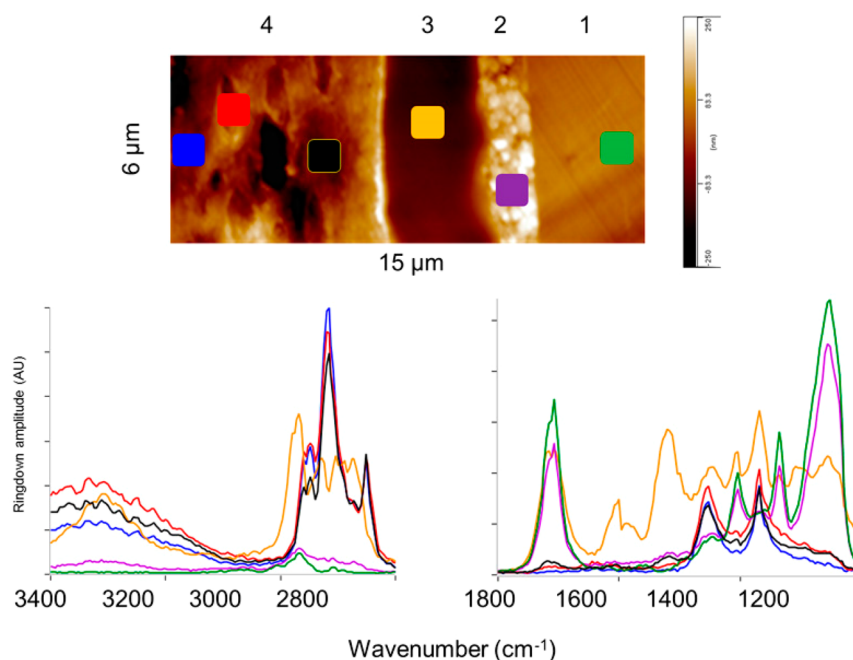


**Figure 11.** AFM-IR analysis performed in the reverse engineering of the top four layers of a laminated polymer multilayer film. AFM-IR spectra were obtained for each layer, and the resulting spectra were compared against reference FT-IR spectra to identify the layer composition. Reprinted with permission from ref 52. Copyright 2012 John Wiley and Sons.

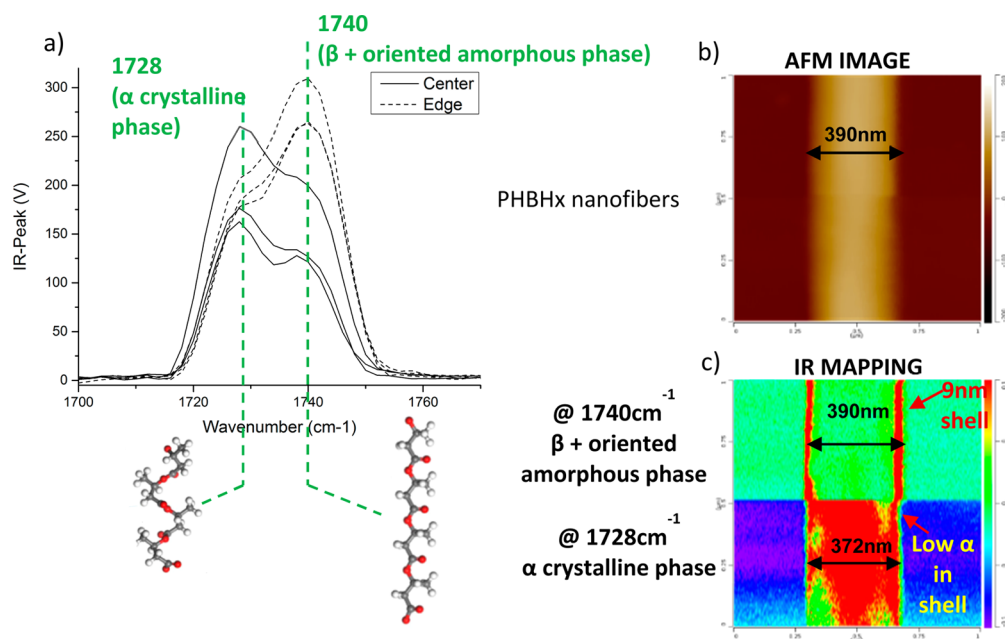


**Figure 12.** AFM-IR measurements of electrospun fibers reveal the distribution of two different conformations of the polymer, a crystalline phase and an amorphous phase. (a) AFM-IR spectra at the edge and center of a PHBHx nanofiber. The spectra have different absorption peak positions corresponding to the two polymer phases. (b) AFM image of a nanofiber. (c) AFM-IR mapping of the nanofiber at two different frequencies, top at 1740  $\text{cm}^{-1}$ , corresponding to the amorphous phase and bottom at 1728  $\text{cm}^{-1}$  corresponding to the crystalline phase. The IR mapping and spectroscopy reveal a 9 nm shell containing a higher concentration of the amorphous phase. Adapted from ref 55. Copyright 2015 American Chemical Society.

study electrospun fibers made from a biodegradable polymer (poly(3-hydroxybutyrate-*co*-3-hydroxyhexanoate, PHBHx). AFM-IR analysis of individual nanofibers revealed the presence of two distinct phases of PHBHx, one amorphous and one crystalline. As shown in Figure 12, the AFM-IR analysis distinguished the two phases based on distinct spectroscopic features, including different peak positions of the carbonyl

absorption band. Further, AFM-IR imaging demonstrated a spatial segregation of the two phases into a core-shell structure, with a higher concentration of amorphous phase and a newly discovered  $\beta$  phase in the shell and a higher concentration of crystalline phase in the nanofiber core.

**3.1.4.2. Molecular Orientation in Fibers.** AFM-IR has also been used to study molecular orientation effects in fibers.<sup>4</sup> The

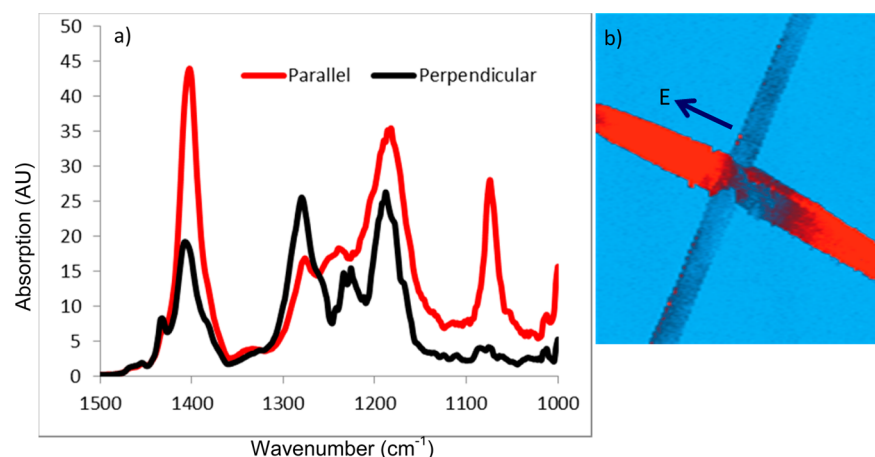


**Figure 13.** AFM-IR measurements of highly oriented PVDF fibers under variable polarization provides information about molecular orientation. (a) AFM-IR spectra at two orthogonal polarizations. (b) AFM-IR absorption image of two crossed PVDF fibers obtained at  $1404\text{ cm}^{-1}$ . The fiber oriented with the electric field of the incident radiation shows significantly higher IR absorption associated indicating alignment of  $\text{CH}_2$  wagging and C–C antisymmetric stretching bonds with the fiber axis. Reprinted with permission from ref 4. Copyright 2012 OSA Publishing.

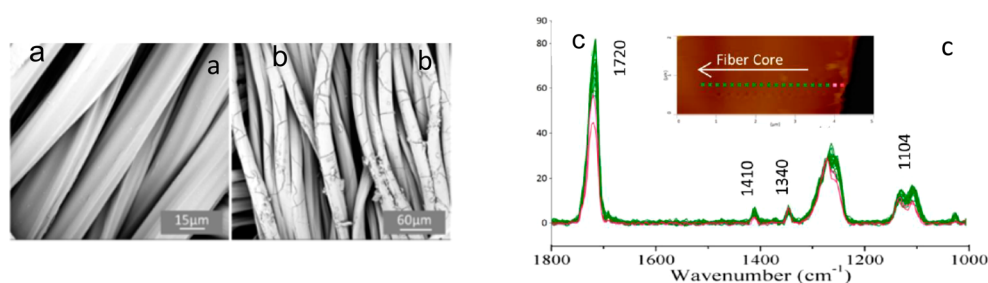


**Figure 14.** AFM-IR investigation of vapor infiltration into PET fibers with trimethylaluminum. AFM-IR spectra provide insights as to the nature of chemical changes induced by the vapor treatment and the depth of penetration of the treatment. (a–b) TEM images of PET fibers (a) before and (b) after treatment. (c) Array of AFM-IR spectra taken across a cross section of a vapor treated fiber. Adapted with permission from ref 64. Copyright 2014 Cambridge University Press.

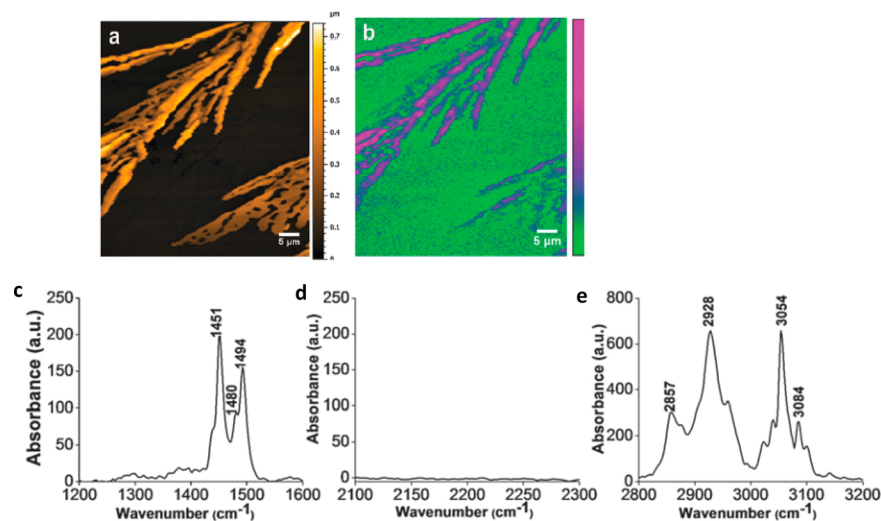


**Figure 15.** AFM-IR measurements of photosynthesized PDPB polymer nanostructures. (a) Conventional AFM image. (b) AFM-IR absorption image at  $1490\text{ cm}^{-1}$ . (c–e) AFM-IR spectra of the PDPB polymer recorded over different spectral regions. The high spatial resolution of the AFM-IR technique compared to classical FT-IR measurement enables identification of lower intensity bands present in the polymer structure induced by photoirradiation. Adapted from ref 65. Copyright 2015 RSC Publishing.

polarization of the incoming IR beam can be varied to enable studies of molecular orientation. Specifically, if the polarization is arranged such that the incident electric field is aligned with the orientation of specific molecular bonds, the absorption by

those bonds will increase providing a stronger AFM-IR signal. Figure 13 shows an example of AFM-IR spectra and an absorption image of highly oriented PVDF fibers. The spectra obtained at two orthogonal polarizations show which molecular

bonds have a specific orientation relative to the fiber axis (as opposed to a random orientation). The AFM-IR absorption image was obtained at  $1404\text{ cm}^{-1}$  associated with  $\text{CH}_2$  wagging, and C–C antisymmetric stretching vibrational motions, indicate that these bonds are aligned along the fiber axis.

**3.1.4.3. Vapor Infiltration into Fibers.** AFM-IR has also been used to study vapor infiltration in fibers (i.e., the depth to which a chemical treatment penetrates from the surface into the bulk of a fiber material).<sup>64</sup> Figure 14 shows examples of measurements on PET fibers that have been treated with sequential vapor infiltration with trimethylaluminum.

**3.1.5. AFM-IR of Conducting Polymer Materials.** AFM-IR has also been used to study a variety of conducting polymeric materials. The one-dimensional conducting polymers seem particularly attractive as their surface-to-volume ratio are very high, making them good potential materials for applications in optoelectronics and nanodevices. Figure 15 shows AFM-IR spectra and absorbance images of photo-synthesized poly(diphenylbutadiyne) (PDPB) nanostructures.<sup>65</sup> These measurements were used to confirm the completion of photopolymerization via the absence of any absorption at  $2146\text{ cm}^{-1}$ , corresponding to the unpolymerized 1,4-diphenylbutadiyne (DFB) monomer. Additionally, the spatial and spectral sensitivity of the AFM-IR technique was able to reveal subtle absorption bands associated with the photopolymerization process. The advantage, in this study, is also to precisely monitor the polymerization at the sub-micrometer scale and to associate the morphology of the polymer to its chemical composition.

Figure 16 illustrates another example application where AFM-IR has been used in the characterization of conducting

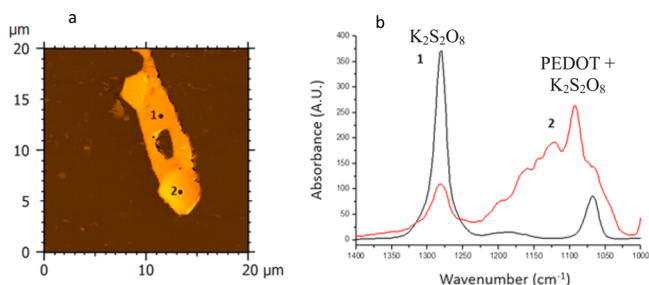


**Figure 16.** AFM-IR characterization of PEDOT polymer nanostructures synthesized by electron beam irradiation in the presence of  $\text{K}_2\text{S}_2\text{O}_8$ . (a) AFM topographic image. (b) AFM-IR spectra recorded at positions 1 and 2 of image (a). From the spectra, region 1 is confirmed to be exclusively inorganic salt, whereas position 2 contains both salt and polymerized PEDOT material. Reprinted with permission from ref 66. Copyright 2016 Elsevier.

polymer synthesis.<sup>66</sup> In this case, electron beam irradiation was used to synthesize conducting poly-(3,4-ethylenedioxythiophene) (PEDOT) nanostructures in an aqueous solution consisting of  $\text{K}_2\text{S}_2\text{O}_8$  and EDOT monomers. The AFM-IR imaging and spectroscopy is able to readily probe the chemical composition of PEDOT nanostructures to discriminate between polymeric regions and the inorganic salt.

**3.1.6. AFM-IR Applications in Medical Devices/Failure Analysis.** A major concern in the medical device industries is the stability and the aging effects of polymers used for medical purposes. Many hospital devices are in contact with body fluid (catheter, blood bags, etc.) or with infusion solutions (tubing) and can be subject to degradation over time. Many medical

devices include parts made of polyurethane or polyvinyl chloride. The manufacturing processing and stabilization of these polymers can employ additives, which can result in health risks if they leach out of the polymer matrix and/or can degrade the performance of the device.<sup>67,68</sup> The detection of the small molecules is quite difficult as they are in low concentration in fluid or aggregated on device surfaces as nanometer thin film. Some techniques as ToF-SIMS, Raman, and AFM<sup>69–72</sup> have been used and have shown interesting results for this type of detection, but in general, the identification and the localization of molecules at the nanometer scale are complex and difficult. The AFM-IR technique is an attractive tool as the AFM-IR can identify the chemical composition with very high sensitivity, down to the scale of monolayers under some conditions.<sup>23</sup>

Commercial polyurethane catheters (Pellethane 2363 80AE, Dow Chemical) usually contain both antioxidants and lubricants. In this section, we present some results obtained on this kind of polymer. Films of polyurethane (Pellethane 2363 80E, Dow Chemical) were prepared by dissolving the catheter and spin-coating the solution on a silicon wafer.<sup>73</sup> After deposition, the polymer surface showed thin needles around 2–5 nm thicknesses that have been observed in previous work.<sup>72</sup> These deposits are really sensitive to the storage conditions and environment and exhibit changes over time. Thirty days after initial measurements (including transportation by air cargo), no more needles were present on the polymer surface, but a blurry region full of small grains took place showing a phase contrast different from the polyurethane (Figure 17).

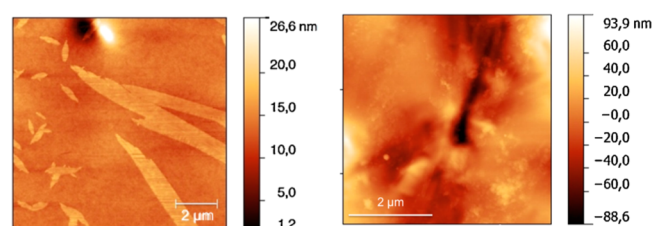


**Figure 17.** Tapping AFM analysis of polyurethane surface. (Left) Initial AFM images in tapping mode of the polyurethane surface (height image on top, phase image on bottom) showing thin needle structures. (Right) AFM images in tapping mode of the polyurethane after 30 days (including airplane transportation of sample) showing a strong different morphology (height up and phase down). Reprinted with permission from ref 73. Copyright 2015 Elsevier.

To characterize this layer composition, we used resonance-enhanced AFM-IR (discussed in section 2.4). Figure 18 shows the topography of the surface showing the blurry region (A) and the clean region of polyurethane (B). For each position, spectra were recorded and clearly reveal the spectroscopic difference between the polyurethane and the unknown film by the addition of 2 new bands at  $1634$  and  $1561\text{ cm}^{-1}$ . These 2 bands perfectly fit with the infrared spectrum of the lubricant (carbonyl of the ethylene bis stearamide). To check the distribution of the lubricant, an infrared map was made at  $1634\text{ cm}^{-1}$ . Figure 19 represents the overlay of the topography (in 3D) with a color code corresponding absorption at  $1634\text{ cm}^{-1}$  (strong absorption in violet and no absorption in green). AFM-IR is able to detect the presence of the lubricant with very high sensitivity, as layers of only 4 nm thickness are clearly visible (red arrows). Moreover, we can spatially distinguish regions with lubricant versus small regions comprising bare polyurethane (areas without purple coloration and indicated by white



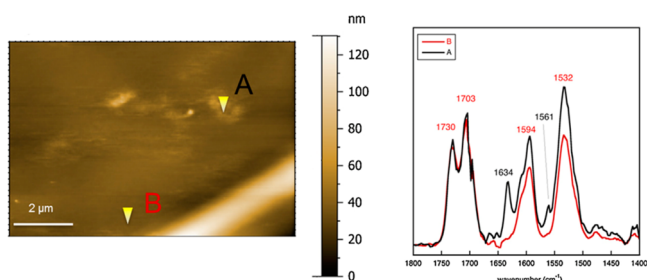


**Figure 18.** AFM-IR analysis of the polyurethane surface 30 days after initial measurement. (left) AFM images of topography from the polyurethane surface modified [(A) unknown deposition; (B) clean polyurethane]. (right) IR spectra obtained on the A and B positions clearly shows the different composition (2 new bands at 1634 and 1561  $\text{cm}^{-1}$ ) of the blurry region (A) compared to the clean polyurethane). Reprinted with permission from ref 73. Copyright 2015 Elsevier.

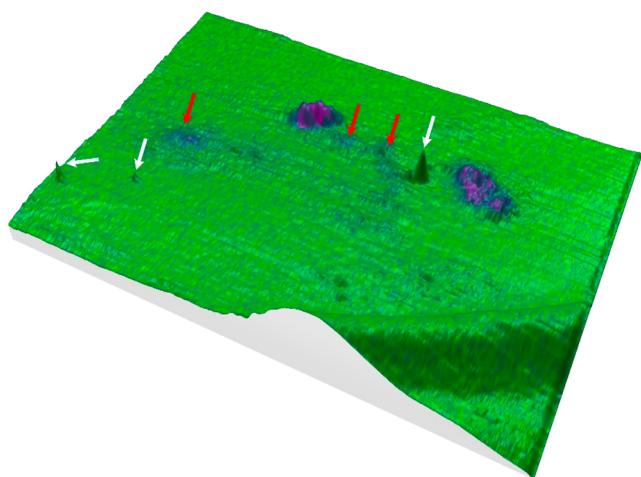


**Figure 19.** Overlay of the topography image (3D) with a color code representing the absorption intensity at 1634  $\text{cm}^{-1}$  revealing the presence of the lubricant on the polyurethane surface (strong absorption violet, no absorption green). Red arrows indicate the location of a very thin amount of lubricant (4 nm thick), and white arrows show some pure polyurethane spots. Image adapted from measurements described in ref 73.

arrows). Resonance-enhanced AFM-IR shows promise as a powerful technique to detect a small amount of molecules, including nanometer scale analytical chemistry, including applications in biocompatibility.

**3.1.7. Coatings.** AFM-IR has also been used to look at a variety of thin films and coatings, including polyimide film on copper<sup>74</sup> and epoxy phenolic films.<sup>75,76</sup>

The Lyons group at the University of Manchester is heavily focused on coatings and corrosion research. The group has investigated water uptake in organic coatings,<sup>75</sup> degradation mechanisms in epoxy phenolic coatings,<sup>77</sup> and the nanoscale chemical heterogeneity in epoxy phenolic formulations.<sup>76</sup> In the latter study, Morsch et al. established that nanoscale nodule features within an epoxy phenolic formulation correspond to heterogeneous network connectivity.<sup>76</sup> Figure 20 shows example AFM and AFM-IR absorption measurements of microtomed epoxy surfaces showing the absorption contrast associated with the nodule regions.

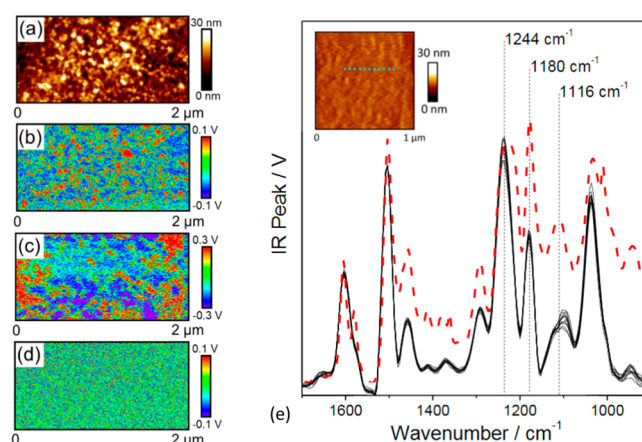


**Figure 20.** AFM-IR investigation of nanoscale nodules in an epoxy phenolic formulation. (a) AFM image of microtomed epoxy surface. (b–d) AFM-IR absorption images collected at (b) 1116  $\text{cm}^{-1}$ , (c) 1244  $\text{cm}^{-1}$ , and (d) 1180  $\text{cm}^{-1}$ . (e) AFM-IR absorption spectra (dark lines) and ATR-FTIR spectra (red dashed line) of epoxy phenolic sample. (d) The absorption peaks at 1180  $\text{cm}^{-1}$  is consistent spatially across the epoxy and also shows no contrast in the absorption image. By contrast, the absorption at 1116 and 1244  $\text{cm}^{-1}$  show substantial variation across the sample surface and specifically show stronger intensity associated with the nodules. The absorption at 1116  $\text{cm}^{-1}$  corresponds to the alkyl out-of-phase C–C–O stretch of secondary hydroxyl groups generated during the epoxy cure. From this investigation, the authors were able to determine the nanoscale nodules that were associated with variations in network connectivity. Reprinted from ref 76. Copyright 2016 American Chemical Society.

### 3.2. AFM-IR Applications in Life Sciences

Infrared microspectroscopy is one of the most powerful techniques to enable chemical identification and localization of particular chemical compounds. The number of applications in different domains of science, such as chemistry, biology, agronomy, and medicine, underline the usefulness of infrared analysis. But the spatial resolution limit of conventional IR spectroscopy of around a few micrometers constrains the applications for heterogeneous materials with micro- and nanoscale structures. The life sciences, however, abound with complex arrangements of materials on the submicron scale. Hence the AFM-IR technique with a spatial resolution extending to the nanometer scale can expand the power of IR microspectroscopy to a wealth of new problems in the life sciences. The AFM-IR technique has already been applied to research problems such as subcellular imaging and spectroscopy, including measurements of bacterial and mammalian cells,<sup>78</sup> viral infected bacteria,<sup>79</sup> lipid light harvesting in plants,<sup>80</sup> PHB production by bacteria,<sup>81</sup> and nanoparticle-cell interactions.<sup>82</sup> Other investigations have involved mineral and protein in bone,<sup>83</sup> single microdroplets containing aggregation-prone proteins,<sup>84</sup> and protein aggregation/secondary structure,<sup>85,86</sup> including links between amyloid aggregation and neurodegenerative disease.<sup>87</sup> In this section, we will overview some of these research areas where the use of AFM-IR spectroscopy and imaging brings new insights and complementary analysis.

**3.2.1. Biodiesel Production.** The AFM-IR technique is providing new insights into the nanoscale production of biofuel precursors via microorganisms. AFM-IR is specifically able to look inside cells and measure and map the distribution of triglyceride vesicles with nanoscale spatial resolution. This mapping and associated spectroscopy is providing researchers

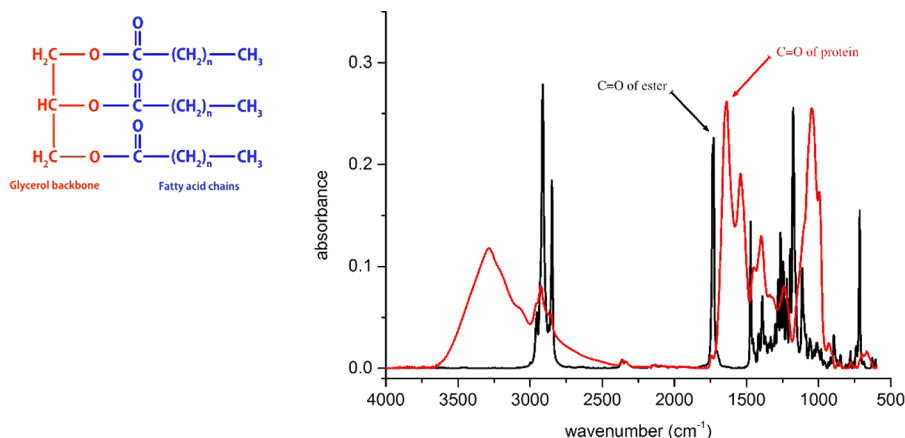


**Figure 21.** (left) Scheme of the triacylglycerol molecule composed of 3 fatty acids and glycerol backbone. (right) In black, FT-IR spectrum of the triacylglycerol molecule showing the CH-stretching modes of  $\text{CH}_2$  and  $\text{CH}_3$  vibrations ( $3000\text{--}2850\text{ cm}^{-1}$ ), the ester carbonyl at  $1740\text{ cm}^{-1}$  and the fingerprint region ( $1500\text{--}1000\text{ cm}^{-1}$ ). In red, FT-IR spectrum of *Streptomyces coelicolor*, showing O–H and N–H stretching modes ( $3500\text{--}2800\text{ cm}^{-1}$ ), CH-stretching mode ( $3000\text{--}2850\text{ cm}^{-1}$ ), amide I and amide II bands (around  $1650$  and  $1540\text{ cm}^{-1}$ , respectively), stretching  $\text{P}=\text{O}$  modes of  $\text{PO}_2$  phosphodiester (antisym at  $1240\text{ cm}^{-1}$  and sym at  $1080\text{ cm}^{-1}$ ).

new tools to understand and optimize emerging techniques for biofuels production.

Biodiesel is an attractive alternative energy source to the petroleum-based diesel fuel. It is usually produced from renewable biomass by trans-esterification of triacylglycerols (TAG)<sup>88</sup> from plant oils. Even if biofuels have benefits versus fossil fuels (less toxic), they are often criticized since they use agricultural land that could be used for food production. As an alternative, producing bio-oils by fermentation of oleaginous microorganisms constitutes an appealing alternative to the use of agricultural lands. The first attempts to engineer biofuel-producing microbes focused on well-known organisms such as yeasts and *E. coli*.<sup>89–91</sup> More recently, biologists also studied some other microbial species (*Streptomyces*) well-known for their ability to grow at an industrial scale and to degrade agricultural waste.<sup>92–94</sup>

Finally, the most explored microorganisms are yeast, fungi, microalgae, and *Streptomyces*.<sup>95–97</sup> Now there is an intense effort to find the best triacylglycerols accumulator. This effort has pushed researchers to find quick and quantitative methods to estimate the TAG production microbial cultures. Usually lipid quantification is carried out by gravimetric methods that are time-consuming and need a significant amount of biomass. Recently Fourier transform infrared (FT-IR) spectroscopy appeared as an alternative method.<sup>98–100</sup> Triacylglycerols are composed of three fatty acids chain bound to a glycerol molecule (Figure 21). The infrared spectrum of this compound is well-known and shows specific infrared bands. Specifically, the CH-stretching bands characteristic of fatty acid chains, particularly  $2912\text{ cm}^{-1}$   $\text{CH}_2$  antisymmetric stretching and  $2849\text{ cm}^{-1}$   $\text{CH}_2$  symmetric stretching, as well as the  $\text{C}=\text{O}$  ester stretching band at  $1727\text{ cm}^{-1}$ . By comparison to a *Streptomyces coelicolor* spectrum (Figure 21), most of the TAG bands are overlapping and only the ester band is significant. As a consequence, the presence of the ester band in a biosample spectrum will be an indicator of the TAG production. Moreover, as the amide I band ( $1638\text{ cm}^{-1}$ ) represents the protein signature of the biomass, the ratio of ester and amide gives directly a quantitative estimation of the lipid production. As the FT-IR analysis is fast and does not require a large amount of biomass, the study of a particular microorganism cultures can be extensively performed over hundreds of

different strains. Even this kind of analysis gives researchers a good insight into the global production of TAG but does not allow a detailed understanding of the localized production process within bacterial cells.

The AFM-IR technique, however, gives direct insights into the TAG accumulation directly inside the cell, down to the scale of individual nanosized TAG vesicles. The knowledge of the local accumulation can give compelling information about the metabolic process of the cell. An additional advantage of the AFM-IR technique is the ability to detect the absorption under the surface of the sample and even for samples thicker than micrometer. Figure 22 shows different examples of TAG detection inside different microorganisms (*Streptomyces*, yeast, microalga) and their corresponding spectra. Usually the TAG accumulation is not diffuse into the body of the microorganism but stored in a vesicle. In all IR mapping ( $1740\text{ cm}^{-1}$ ), we can identify clearly the absorption of the vesicles. Most of the time the vesicles have a round shape stabilized by a protein shell ( $1650\text{ cm}^{-1}$ ). The vesicle size depends on the organism and species (e.g.,  $100\text{ nm}$  to  $1\text{ }\mu\text{m}$  for *Streptomyces* and up to  $2\text{ }\mu\text{m}$  for microalga). The infrared spectra of the vesicles look highly similar, the presence of the ester carbonyl identifying the TAG associated with the amide I band corresponding to the proteins surrounding the vesicles. For the larger vesicles of microalga, the amount of TAG is so big that the amide I is just a shoulder on the side of the ester carbonyl. One can notice the ability of the technique to detect big vesicles buried deeper under the surface (diameter of microalga are around  $2\text{ }\mu\text{m}$ ) due to the intense expansion produced. This ability is really unique in the infrared near-field domain, as scattering s-SNOM (scattering near-field microscopy) or TERS (tip enhanced Raman scattering) can probe only a few nanometer around the AFM tip, leading this type of study to not detect any TAG signal coming from the vesicles.

By doing statistical analysis of one specific culture at a specific time, it is possible to obtain the distribution of the vesicles production.<sup>101</sup> This type of analysis can be used to compare the distribution in function of time or can be used to compare different strains at the same time. This type of approach is complementary with GC/MS, proteomic, and FT-IR for providing understanding of the metabolism of *Streptomyces*. This type of research is expanding through

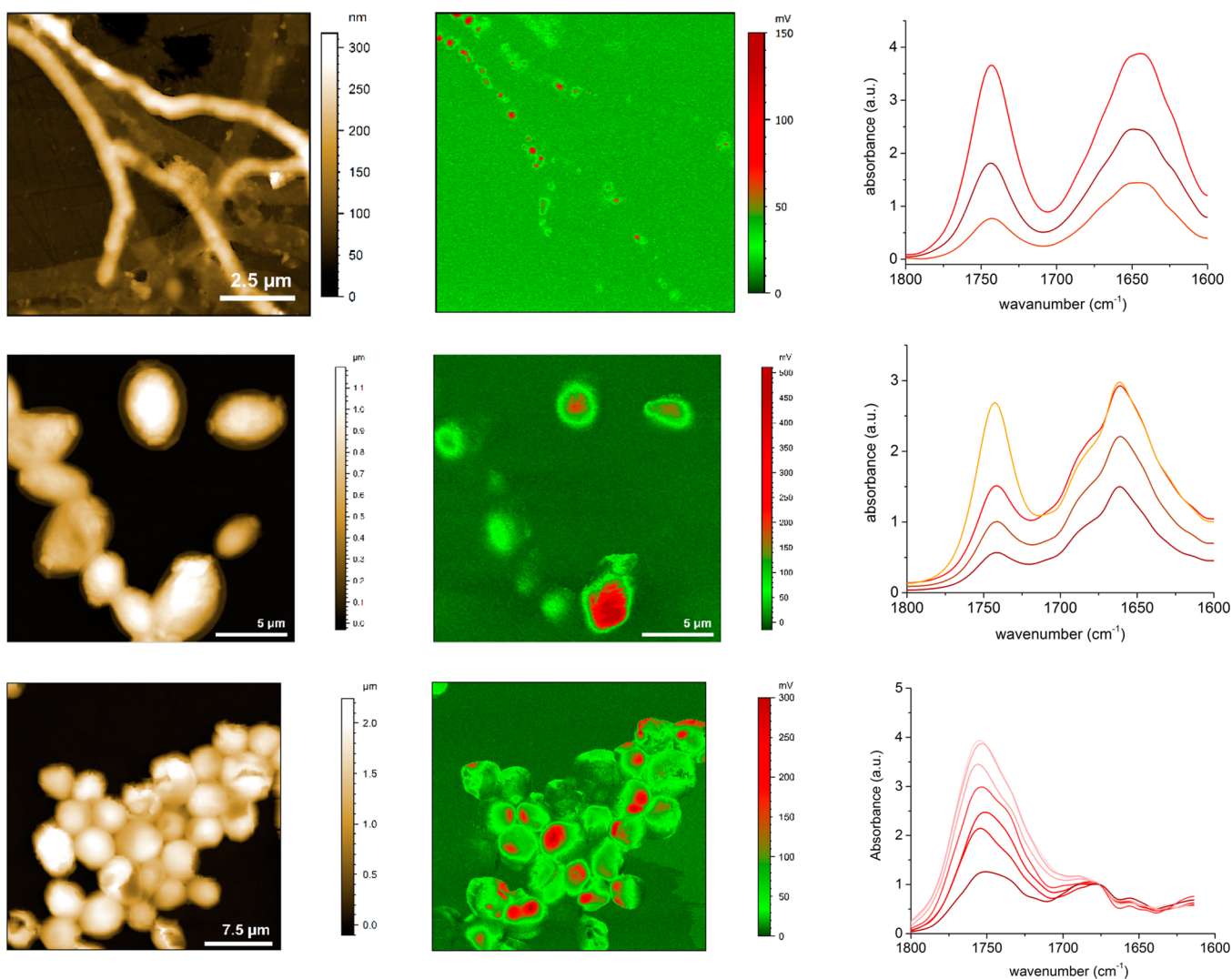


**Figure 22.** AFM topography, AFM-IR map at 1740 cm<sup>-1</sup> revealing the presence of TAG (triacylglycerol), and AFM-IR spectroscopic measurements of the corresponding TAG vesicles. The samples are respectively from the top to bottom: the bacterium *Streptomyces*, the yeast *Yarrowia*, and the microalga *Parachlorella Kessleri*. This comparison clearly shows that the amount of TAG produced by the alga is really huge, as the vesicles have the biggest size (more than 2 μm) and as spectra show an ester carbonyl band so intense that the amide I is seen as a small shoulder on the side (ratio about 8).

ongoing collaborations and is expected to provide key insights into biofuel production mechanisms.

**3.2.2. Single Cells and Infrared Tags.** The subdiffraction-limited spatial resolution of AFM-IR is really attractive for cell studies. Conventional IR microspectroscopy is extensively used for biomedical applications,<sup>102–104</sup> including imaging cells. This interest has grown recently in part due to the integration of synchrotron IR sources with IR microspectroscopy and due to improvements in IR detectors.<sup>105,106</sup> Infrared spectra can detect the cell type, physiological status, disease state, and even environment reactions of the cell or a specific organelle. Despite these advances, many biological phenomena like protein production in the endoplasmic reticulum, chromatin transformation in the nucleus, or degradation in lysosome occur on length scales well below the resolution limit of conventional IR microspectroscopy. There is a strong push to achieve a better spatial resolution than conventional FT-IR microscopes. Organelles are typically detected in cells through the use of fluorescent microscopy (around 200–500 nm resolution), but this approach requires staining with fluorescent markers. S.

Clède et al. have demonstrated an interesting method for detecting organelles by IR<sup>107</sup> that avoids the limitations of staining, but it is constrained by the spatial resolution limitation of the conventional IR microspectroscopy, with a minimum pixel size of >3 μm. AFM-IR can achieve spatial resolutions better than 50 nm, leading to much finer IR mapping of organelles and more highly resolved spectra. Figure 23 shows topography and the IR map of a fixed MCF-7 cancer cell for amide I band (proteins) and phosphate band (DNA, RNA) with a pixel size of 130 nm. These measurements were made with cells incubated on a CaF<sub>2</sub> window. This window is then placed on a CaF<sub>2</sub> prism followed by illumination by IR radiation from below via a total internal reflection scheme. This illumination scheme can probe the full thickness of the sample as light is effectively coupled from the prism into the cell. To avoid reflection losses from air interfaces between the CaF<sub>2</sub> prism and window, a thin oil film is deposited between the prism and the window as an index matching layer. A deuterated oil was selected to avoid overlapping absorption bands with the regions of interest in the sample.<sup>108</sup>



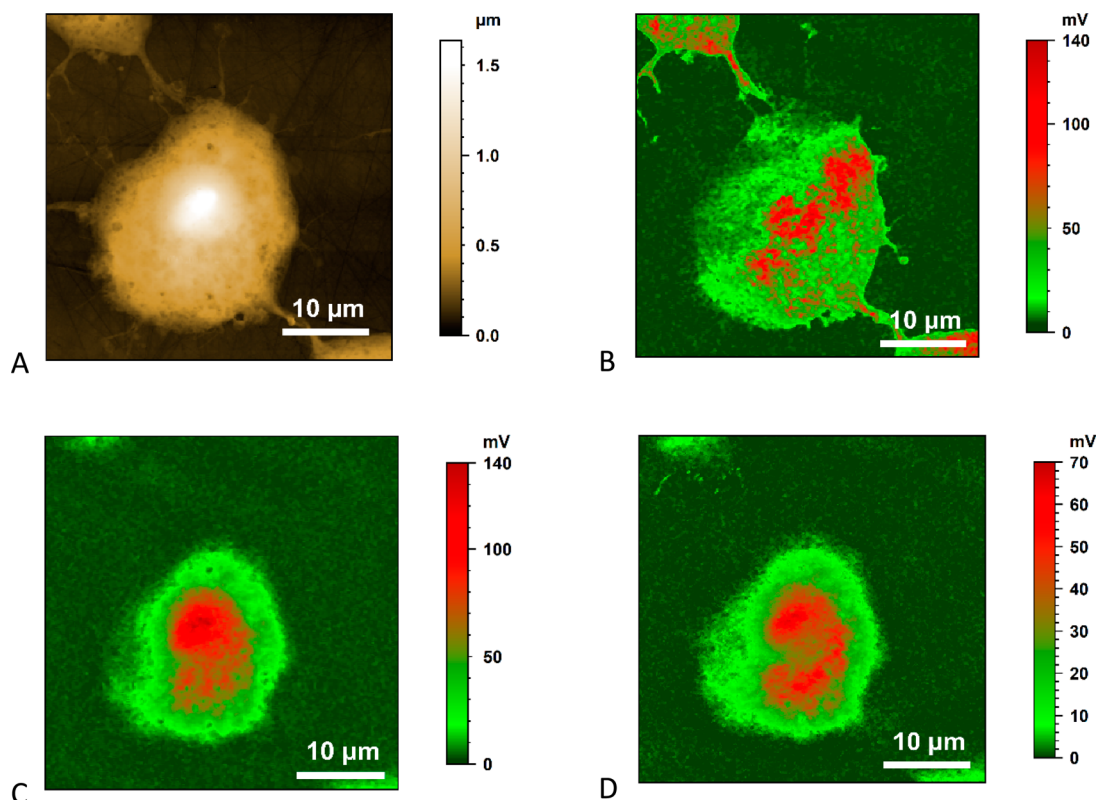


**Figure 23.** AFM-IR analysis of MCF-7 breast cancer cell. (A) AFM topography of a fixed MCF-7 cell. (B) Corresponding AFM-IR map at  $1650\text{ cm}^{-1}$  (amide I band vibration) related to the protein concentration. (C) Corresponding AFM-IR map at  $1080\text{ cm}^{-1}$  (symmetrical  $\text{P}=\text{O}_2$  stretching vibration) related to the DNA and RNA distribution. (D) Corresponding AFM-IR map at  $1925\text{ cm}^{-1}$ , revealing the infrared probe (metal-carbonyl) presence. This specific map is different from the other maps and indicates without ambiguity the location of the molecule of interest.

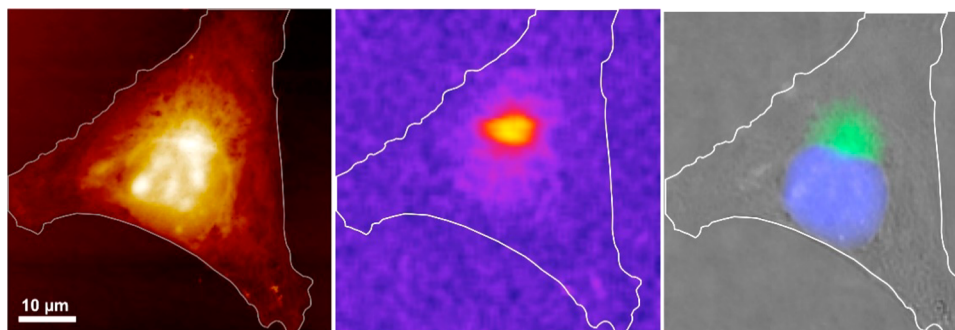


**Figure 24.** Correlative AFM-IR and fluorescence analysis. (left) AFM topography of a breast cancer cell MCF-7 fixed and air-dried. (middle) AFM-IR mapping at  $1920\text{ cm}^{-1}$  corresponds to mestranol location (metal-carbonyl infrared probe). (right) Fluorescence imaging where bright field image is merged with nucleus (DAPI, blue) and luminescence of the Scompi probe (green). The white line follows the contour of the cell as an indicator. The AFM-IR signal and fluorescence signal are perfectly correlated, but the sensitivity of the AFM-IR makes its location more contrasted into the cell. Reprinted with permission from ref 108. Copyright 2013 The Royal Society of Chemistry.

The advantage of the AFM-IR spatial resolution has also been shown by the group of C. Polcar (ENS Paris) on cancer cell studies. This group has specific expertise in click chemistry, and they have combined the properties of an organometallic molecule (rhenium-carbonyl) with a hormone structure to verify that the concentration of this compound was mainly located inside the nucleus of human cancer cells (MDA-MB-231). One of the interesting properties of this particular metal-carbonyl is that it has two characteristic infrared absorption bands at  $1925$  and  $2017\text{ cm}^{-1}$ . These bands are conveniently away from other common absorptions in biological materials, so this molecule can act as a very effective small molecule tag,<sup>109</sup> enabling the location of the molecule of interest via

detection and imaging of IR absorption bands at  $1925$  and  $2017\text{ cm}^{-1}$ . Using this kind of approach the location of molecules of interest after treatment and fixation of the cell culture can be determined without ambiguity (Figure 23).

Fluorescence microscopy is the most commonly used technique for biochemically specific optical imaging because of its spatial resolution and the numerous variety of tags available to label specific target molecules. The group of C. Polcar has developed a bimodal probe that allows localization by both IR and visible light excitation. This has been achieved by clicking the recarbonyl molecule to 4-(2-pyridyl)-1,2,3-triazole to add visible light luminescence, while preserving the recarbonyl IR absorption bands mentioned above. This new

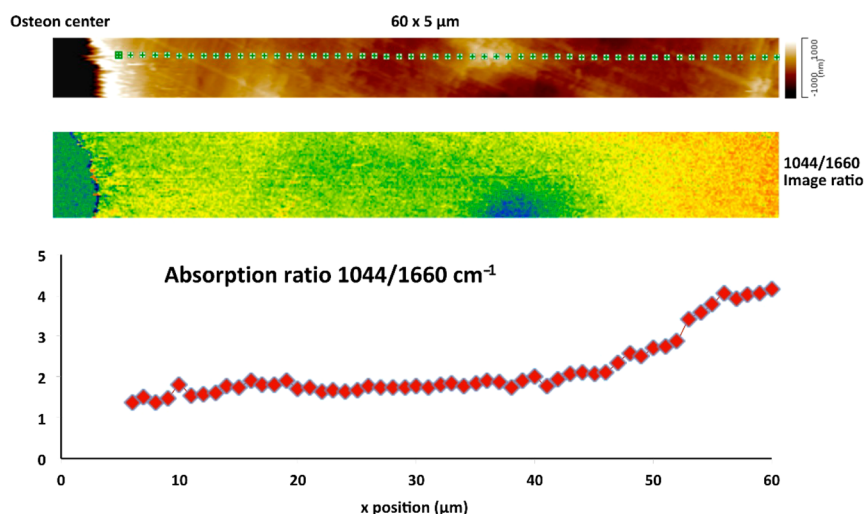


**Figure 25.** AFM-IR analysis of Osteon sample. (Top) AFM map of 60  $\mu\text{m}$  from the osteon center with markers indicating where AFM-IR spectra were obtained. (Center) Image showing a map of the ratio of 1044/1660  $\text{cm}^{-1}$ , corresponding to the ratio mineral/protein reveals a higher concentration of protein close the center of the osteon. (Bottom) Intensity ratio of the 1044/1660  $\text{cm}^{-1}$  AFM-IR spectral bands along a line extending from the osteon center (top). Reprinted with permission from ref 83. Copyright 2014 Springer.

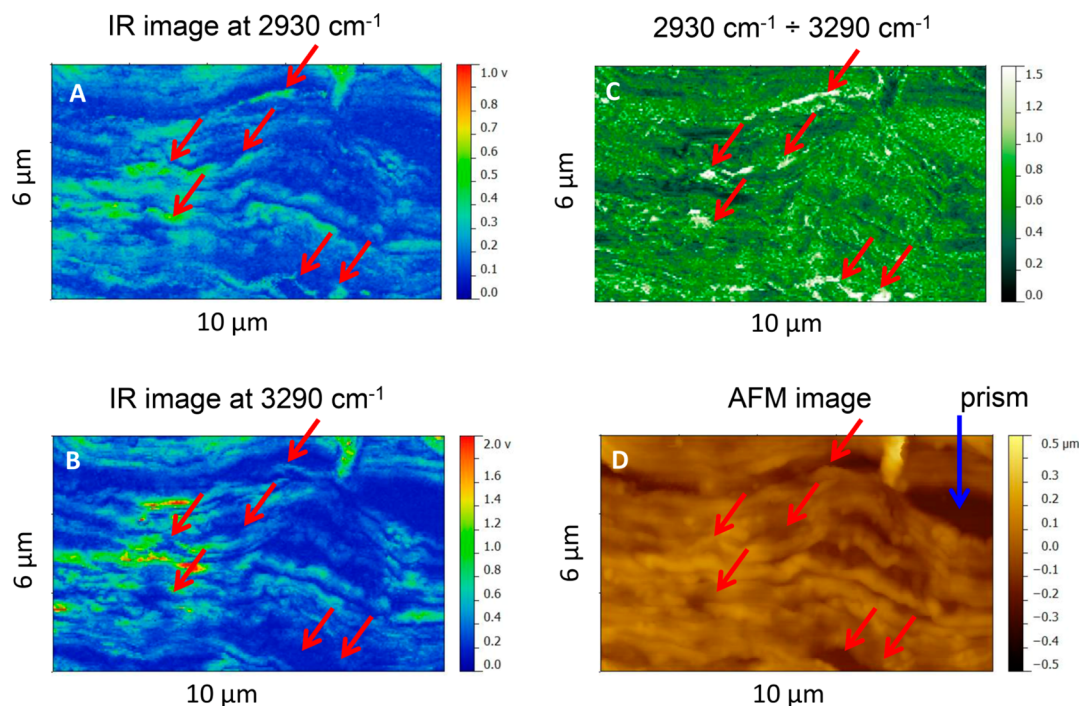


**Figure 26.** AFM-IR analysis of skin sample. (A) AFM-IR map at 2930  $\text{cm}^{-1}$  of the  $\text{CH}_2$  stretching vibration used to localize the lipids. (B) AFM-IR map at 3290  $\text{cm}^{-1}$  of the  $\text{NH}$  stretching used to localize the protein. (C) Corresponding ratio image 2930/3290  $\text{cm}^{-1}$ , revealing the region of high lipid concentration (red arrows). (D) AFM topography of the corresponding stratum corneum sample. Reprinted with permission from ref 110. Copyright 2013 John Wiley and Sons.

molecule, called SCoMPI, is a powerful tool to make IR-visible correlative imaging.<sup>108</sup> Figure 24 shows a topographic image of a cancer cell (left), an AFM-IR absorbance image (center), and a visible light luminescence emission (right) of the same cell. The visible image at the right shows the region in blue that corresponds to the cell nucleus stained by conventional DAPI fluorescent staining as well as the distribution of the mestranol hormone (shown in green), as detected by AFM-IR via the recarbonyl absorption. The luminescence emission from the SCoMPI tag in the visible comes from exactly the same location on the cell as the IR absorption, but the AFM-IR image reveals

significantly tighter localization due to the detection of the IR absorption with the AFM tip in a manner than is not limited by convention optical diffraction limits. With this study, we clearly see that the mestranol penetrates into the Golgi apparatus, but the concentration seems too small to be detected into the nucleus. This example shows that the correlation of IR and visible images is a powerful technique that combines the high resolution of the AFM-IR to detect the molecule of interest and organelle identification done by the fluorescence technique. With the increase of the sensitivity of the AFM-IR technique,



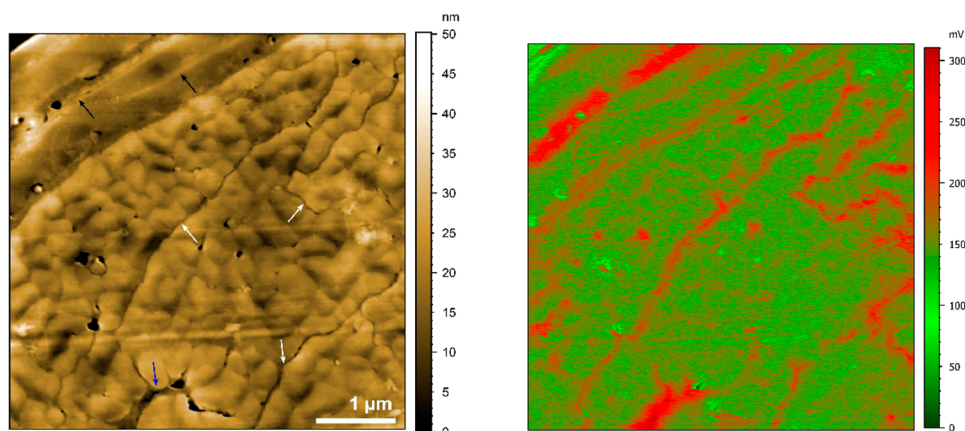


**Figure 27.** AFM-IR analysis of 2 virgin hair thin sections. (left) AFM topography of hair thin section, where the cortex and the cuticle are clearly distinguished by their different morphology. White arrows indicate the location of the cell membrane complex of the cortex, black arrows indicate the location of the endocuticle, and a blue arrow shows the location of a nuclear remnant. (right) Corresponding IR map at  $2934\text{ cm}^{-1}$  ( $\text{CH}_2$  antisymmetric stretching band) revealing regions of high concentration of lipids (in red). Sample courtesy of L. Bildstein, L'OREAL France.

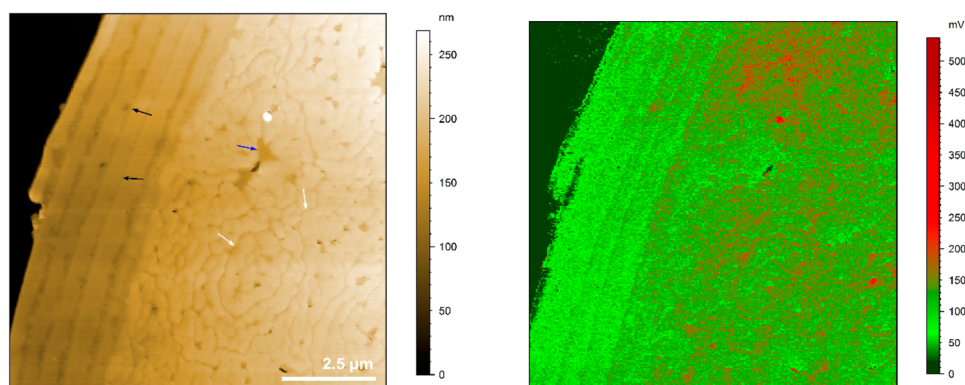


**Figure 28.** AFM-IR analysis of a delipidised hair thin section. (left) AFM topography where white arrows indicate the location of the cell membrane complex of the cortex, black arrows indicate the location of the endocuticle, and a blue arrow shows the location of a nuclear remnant. (right) Corresponding IR map at  $2934\text{ cm}^{-1}$  ( $\text{CH}_2$  antisymmetric stretching band) showing where the lipids are concentrated (red). Sample Courtesy of L. Bildstein, L'OREAL France.

the goal is now to detect very low concentration of hormones typically under  $1\text{ }\mu\text{M}$ .

**3.2.3. Tissue.** AFM-IR has also been used on various tissue samples, including bone, skin, and hair, revealing the distribution of lipids, proteins, minerals, and chemical additives. In the case of calcified tissue, the AFM-IR technique has been used by S. Gourion-Arsiquaud et al.<sup>83</sup> to map the relative distribution of biopolymer versus mineral in the complex structure of bone. As shown in Figure 25, the researchers in this study used AFM-IR imaging and spectroscopy of an osteon region of bone to quantify the mineral concentration (via the phosphate band at  $1044\text{ cm}^{-1}$ ) versus the biopolymer matrix concentration (via amide I band associated with protein absorption at  $1660\text{ cm}^{-1}$ ). The relative amounts of mineral and protein can be determined by the ratio of these two absorption bands. Mapping this ratio as a function of distance from the osteon center reveals an increased relative concentration of biopolymer close to the blood supply at the osteon center that decreases moving away from the center.

C. Marcott et al. have used the AFM-IR technique in collaboration with L'Oréal to provide nanoscale chemical mapping on human tissue like skin and hair.<sup>110</sup> In these research areas, there is a strong interest in the mapping of various biomolecules as well as detailed understanding of how

and where various skin and hair treatments penetrate into and localize within the target material. There is high interest in chemical composition and mechanical properties of such tissue especially related to understanding how to optimize how drugs and other treatments interact with hair or skin.

In one study, AFM-IR was used to study samples of human stratum corneum, the outermost layer of the epidermis. The main role of this layer is to act like a barrier against foreign substances. The stratum corneum is composed of corneocytes cells inside an intercellular lipid matrix. Corneocytes are cells without nuclei filled with keratin filaments, amino acids, and other small molecules. It is commonly believed that the drugs can penetrate the stratum corneum only through the thin lipid matrix. The possibility to map precisely the distribution of lipids around the corneocytes cells will give an important knowledge to better understand how the drugs pass the stratum corneum barrier.

In the work by Marcott et al., AFM-IR was used to map the distribution of protein and lipids on a microtomed section of a human abdominal skin (Figure 26). To detect the concentration of lipid on the layer, two different IR maps have been recorded: one at  $3290\text{ cm}^{-1}$  centered on the amide A band ( $\text{NH}$  stretching) of protein and the other at  $2930\text{ cm}^{-1}$  ( $\text{CH}_2$  antisymmetric stretching) more characteristic to the long



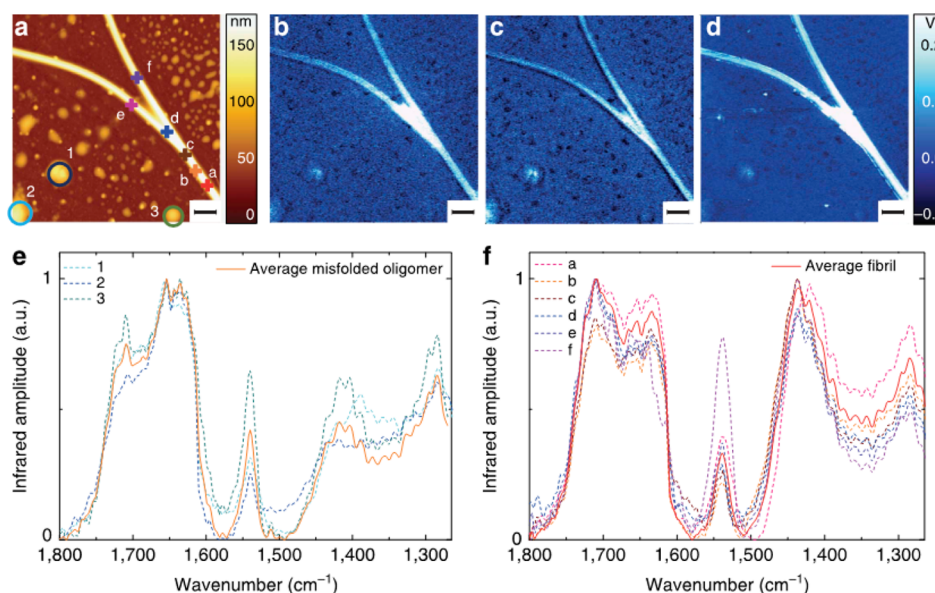


**Figure 29.** AFM-IR analysis of Josephin protein aggregation. (a) AFM topography of the protein aggregation showing fibrillar and oligomeric structures. Corresponding infrared absorption map at (b)  $1700\text{ cm}^{-1}$ , (c)  $1655\text{ cm}^{-1}$ , and (d)  $1430\text{ cm}^{-1}$ , with the scale bar at  $1\text{ }\mu\text{m}$ . Spectra of amyloid structures: (e) misfolded oligomer labeled 1, 2, 3 in (a) show a strong absorption at  $1655\text{ cm}^{-1}$  compared to  $1700$  and  $1430\text{ cm}^{-1}$ , and (f) fibrils labeled a–f in (a) show the opposite behavior linked to the  $\beta$ -turn concentration increase. Reprinted with permission from ref 86 under Creative Commons Attribution 4.0 International License. Copyright 2015 Nature Publishing Group.

hydrocarbon chains. The IR absorbance image ratio of these two wavenumbers point out the region where the lipids are at the highest concentration. First, these locations are all found at the periphery of the corneocytes cells as was predicted, but interestingly, the lipid concentration is not uniform throughout the matrix and seems to have specific regions of high concentration. This part of the study is a first step and shows the ability to obtain relevant information at the hundred-nanometer scale, suggesting the utility of the AFM-IR technique for drug penetration studies.

C. Marcott et al. in collaboration with L'Oréal have also characterized the lipid distribution thin cross sections of natural hair with AFM-IR.<sup>111</sup> In this work, the researchers found that the medulla has the highest lipid concentration compared to the cortex or the cuticle. But these lipid concentrations are not homogeneous and show high concentrations in the intercellular spaces of the cortex. On the basis of these first results showing the efficiency of AFM-IR, L. Bildstein et al. showed the differences between lipid distribution for a virgin and delipidized hair coming from the same batch of hair. Figure 27 shows topographic and IR absorption images of two thin sections of the reference hair (untreated). AFM-IR absorption was measured at  $2934\text{ cm}^{-1}$  ( $\text{CH}_2$  antisymmetric stretching corresponding to the lipid). The study clearly detected the lipid concentration in the CMC (cell membrane complex) of the cortex (white arrow) and in the endocuticle (black arrows) with a better resolution (around  $20\text{--}50\text{ nm}$ ), moreover, the nuclear remnants are easy to identify (blue arrow) in the cortex and displayed also a very high lipid concentration. The delipidization impact on the hair is clearly put in evidence in Figure 28. The lipid concentration in the cuticle has diminished (light green) and the endocuticle shows no strong lipid absorbance (black arrows), while the lipids in the cortex (CMC, white arrows) have not been really affected by the solvent extraction (chloroform/methanol mixture). This study of delipidization of the hair tissue at this scale is unprecedented in terms of chemical analysis of complex tissue. The AFM-IR absorbance

images clearly provide a better understanding at the nanometer scale that the delipidization process has only removed most of the lipids in the cortical CMC and that the nuclear remnants in the cortex are not really affected by the lipid extraction process.

#### 3.2.4. Protein Aggregation and Secondary Structure.

AFM-IR has also been used to study protein aggregation and secondary structure, with the specific goals of providing new insights into diseases related to protein misfolding. Aggregation of proteins has been extensively studied, particularly the fibrillar protein aggregates called amyloids which seem connected to neurodegenerative diseases like Parkinsons, Alzheimers, and Huntingtons. In nature, not all amyloids' forms are pathological and in fact can be functional.<sup>112,113</sup> As such understanding of the aggregation process and their consequence in the organism is essential to predict and cure disease.

Amyloids are the result of monomeric protein aggregation that transforms their internal arrangement, leading to a fibril form with a characteristic  $\beta$ -sheet structure. This conformation is completely different from the monomeric one and is usually difficult to disassemble. Strong evidence exists indicating that the toxicity and the pathological properties come from an intermediate form of fibrils rather than the amyloid itself. Moreover, one of the important questions is to know if the  $\beta$ -sheet is the consequence of the aggregation or initiates it. All these aspects show that the problem is not easy and seems to be at the early stage of comprehension, which is why it is important to develop effective experiments and powerful tools to be able to characterize precisely the protein aggregation. F.S. Ruggeri et al. have used the AFM-IR technique because of its ability to acquire nanometer scale infrared spectra.<sup>86</sup> The researchers have worked on a specific protein, the Josephin domain of the ataxin-3 responsible for the spinocerebellar ataxia of type 3. The current hypothesis is that this protein seems to not unfold before aggregation but unfolds only at an advanced stage. As there was previously no way to investigate the intermediate structures that precede the formation of the final fibrils, the AFM-IR technique looked to be a perfect approach.

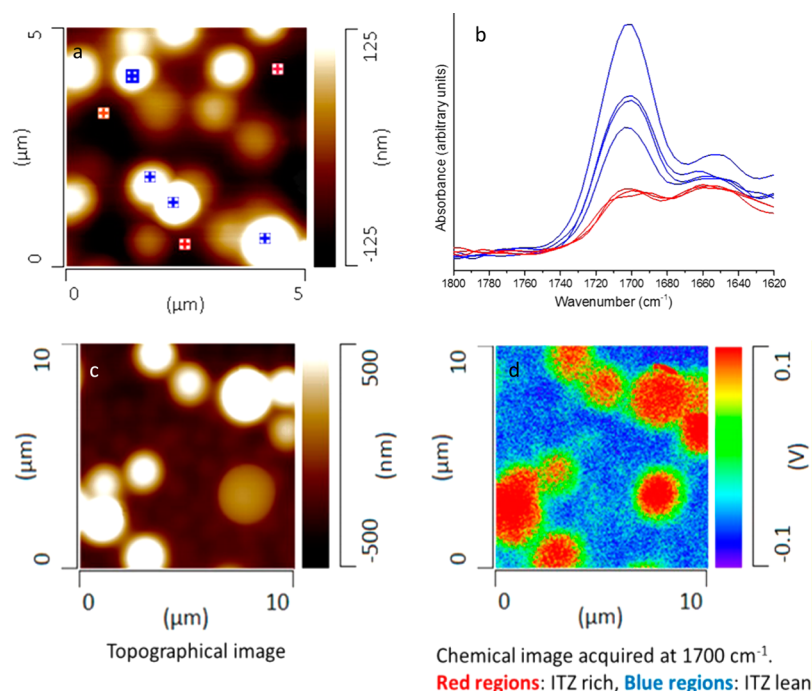


**Figure 30.** AFM-IR measurements of an amorphous solid dispersion of drug/polymer blend consisting of the drug itraconazole (ITZ) and polymer hydroxypropyl methylcellulose (HPMC). (a) AFM topographic image and (b) AFM-IR spectra obtained from a 10% drug/90% polymer blend film). Colored markers on the (a) AFM image indicate locations where the spectra (b) were obtained. The ITZ drug has an IR absorption at  $1700\text{ cm}^{-1}$  that allows identification and mapping of the drug. (c) AFM topographic image and (d) AFM-IR chemical image of a 30%/70% drug/polymer formulation. The IR absorption image at  $1700\text{ cm}^{-1}$  allows clear visualization of the phase separation between polymer and drug. Reprinted from ref 61. Copyright 2015 American Chemical Society.

Indeed, infrared spectroscopy is well-established as a powerful technique for investigating the secondary structure of proteins. The broad amide I band shape, in particular, consists of the superposition of the carbonyl stretching vibrations of various backbone peptide group conformations related to the hydrogen bonding pattern ( $\alpha$ -helix, random coil,  $\alpha$ -turn,  $\beta$ -sheet,  $\beta$ -turn, etc.). The Josephin domain amide I band contains major contributions from  $\alpha$ -helix and random coil conformations.<sup>86</sup> Any change in the infrared spectral band contour of the amide I band will be a good indication that misfolding has occurred. Figure 29 shows a sample after 7 days of incubation with both fibrillar and oligomeric structures present within the field of view. The researchers measured infrared spectra in the  $1800\text{--}1300\text{ cm}^{-1}$  range on a bundle of fibrils of 150 nm thick and some 100 nm size oligomeric assemblies. The infrared spectra confirm that fibril and oligomer have a different secondary structure but one that is also different from the native Josephin domain. In both cases, the fibril and oligomer show stronger absorption at  $1700\text{ cm}^{-1}$  ( $\beta$ -turn) and  $1400\text{ cm}^{-1}$  than for the native form. At this point, it is hard to clearly detect the  $\beta$ -sheet around  $1625\text{ cm}^{-1}$ , as the fibril is not a single fibril but rather an average of hundreds probably in different states of maturation. However, the full results demonstrate the possibility of investigating for the first time the aggregation pathway of the Josephin domain of the ataxin-3, revealing the intermediate nature of the oligomers. This work is the first step toward very challenging studies in biochemistry showing how nanoscale infrared spectroscopy is a useful tool for protein secondary structure analysis.<sup>85</sup> Other recent work by the same group investigated fibrillar aggregates of the first exon of Huntington protein (Exon1) at the single molecule and nanometer scale.<sup>87</sup> AFM-IR chemical images and nanoscale IR absorption spectra,

along with nanoscale morphological and mechanical property analysis are providing new insights into protein aggregation and toxicity in neurodegenerative diseases.

**3.2.5. AFM-IR in Pharmaceutical Sciences.** AFM-IR has been used to study various drug formulations, especially drug polymer blends.<sup>57–60</sup> In pharmaceutical sciences, properties like composition, miscibility, dispersion, phase segregation, and crystallinity can all affect the efficacy and stability of a drug formulation. IR spectroscopy has been widely used in the pharmaceutical sciences for decades, whereas AFM applications have been emerging in recent years. AFM-IR, in combination with related AFM techniques of nanothermal analysis and nanomechanical analysis is providing new correlative measurement analyses to address critical problems in pharma. AFM-IR analysis of drug-polymer blends is providing key insights into drug dispersion, phase segregation, and crystallinity, all of which can affect bioavailability and efficacy of a drug. The Taylor group at Purdue has demonstrated the ability to visualize the distribution of chemical components in drug/polymer formulations.<sup>57–61</sup> In one study,<sup>60</sup> telaprevir-based drug-polymer systems were investigated by AFM-IR at different drug-to-polymer ratios and for three different polymers: HPMC, HPMCAS, and PVPVA. AFM-IR analysis of drug-polymer blends is providing key insights into drug dispersion, phase segregation, and crystallinity, all of which can affect bioavailability and efficacy of a drug. Another study investigated felodipine-poly(acrylic acid) (PAA) blends and revealed submicron domains of an amorphous felodipine-rich phase within a continuous phase rich in PAA.<sup>58</sup> The Taylor group also explored binary blends of poly(vinylpyrrolidone) (PVP) with dextran or maltodextrin of varying molecular weights. AFM-IR evaluation of the blends provided information about the

dependence of polymer molecular weight on chemical composition of the different phases. Another recent study has combined AFM-IR and related AFM-based techniques including nanothermal analysis and nanomechanical spectroscopy to investigate miscibility, phase separation, and local glass transition temperatures of the drug telaprevir with three different polymers and different drug loadings.<sup>60</sup>

Figure 30 shows an example of AFM-IR measurements of a drug/polymer formulation of the drug itraconazole (IZT) and polymer hydroxypropyl methylcellulose (HPMC). By obtaining AFM-IR spectra at different locations on the sample, it was possible to identify different regions as being rich in the IZT drug or rich in the HPMC polymer. Tuning the AFM-IR laser to a specific absorption of the drug, allowed mapping of the relative distribution of the drug. This analysis enabled the visualization of phase segregation between the drug and polymer domains.

Similarly, Figure 31 shows AFM-IR measurements of nanocrystals of an antifungal drug Griseofulvin (GV) dispersed

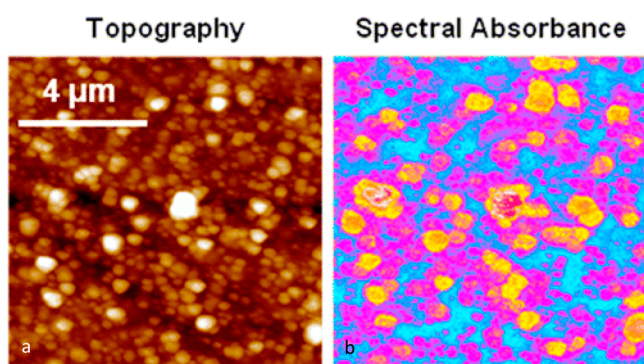


**Figure 31.** AFM-IR analysis of Griseofulvin (GF) particles dispersed in hydroxypropyl methylcellulose (HPMC). (a) AFM topographic image showing the broad GF particle size distribution. (b) Simultaneously obtained AFM-IR chemical image illuminated at  $1625\text{ cm}^{-1}$ ; blue indicates low infrared absorptivity, and pink, yellow, and red indicate areas of GF. Reprinted from ref 59. Copyright 2013 American Chemical Society.

in the polymer hydroxypropyl methylcellulose (HPMC).<sup>59</sup> The AFM-IR chemical map at a characteristic absorption of the drug GV at  $1625\text{ cm}^{-1}$  (corresponding to the C=C bonds in GF)

enables precise mapping of the regions of high concentration of the drug. Drug nanoparticles as small as 90 nm were observed. AFM-IR measurements were also used to estimate the particle size distribution of the GV nanoparticles with good agreement to dynamic light scattering measurements.

### 3.3. Other Applications of AFM-IR

AFM-IR is being used in many other diverse areas, including investigation of metal organic frameworks (MOFs),<sup>114</sup> perovskite solar cells,<sup>115,116</sup> photonics and plasmonics,<sup>117–123</sup> quantum dots<sup>124,125</sup> and semiconductor electronic devices,<sup>126</sup> pharmaceuticals,<sup>57–60</sup> and cultural heritage.<sup>127</sup> This section overviews some of these investigations.

**3.3.1. Perovskite Solar Cells.** Perovskite solar cells are an area of intense research focus in recent years. Perovskite solar cells most commonly employ a hybrid organic–inorganic lead or tin halide-based material as the light-harvesting active layer.<sup>128</sup> Perovskite materials such as methylammonium lead halides are especially provoking increased research interest due to simple manufacturing, low production costs, and dramatically increasing solar cell efficiencies. Perovskite solar cells for example achieved >22% efficiency in 2016 after only 4 years of development, making it the fastest-advancing solar technology to date.<sup>128,129</sup> One of the key issues regarding solar cells is their stability over time. AFM-IR has specifically been used to look at two issues related to perovskite solar cells, including annealing<sup>115</sup> and electromigration.<sup>116</sup> Figure 32 shows an example AFM-IR measurement performed on perovskite solar cells. The images show a cross-section across the anode/cathode region of the cell where the AFM-IR absorption measurement is tuned to an absorption of the methylammonium ion at  $1468\text{ cm}^{-1}$ . AFM-IR absorption images clearly reveal changes in the local concentration of the methylammonium ion due to electromigration when the cell is placed under high bias.

**3.3.2. Photonics and Plasmonics.** AFM-IR has also been used to perform measurements on plasmonic micro- and nanostructures.<sup>117–121</sup> Research in the field of plasmonics has been motivated by the desire to achieve strong localization of electromagnetic fields in the mid-IR and other wavelength regions, for example, to enhance performance of light sources and detectors, as well as enhanced sensors. The Centrone group at NIST fabricated resonant nanostructures for surface-enhanced infrared absorption (SEIRA) applications.<sup>119,120,122</sup>

AFM-IR absorption images at  $1468\text{ cm}^{-1}$  ( $\text{CH}_3$  asym. def.)

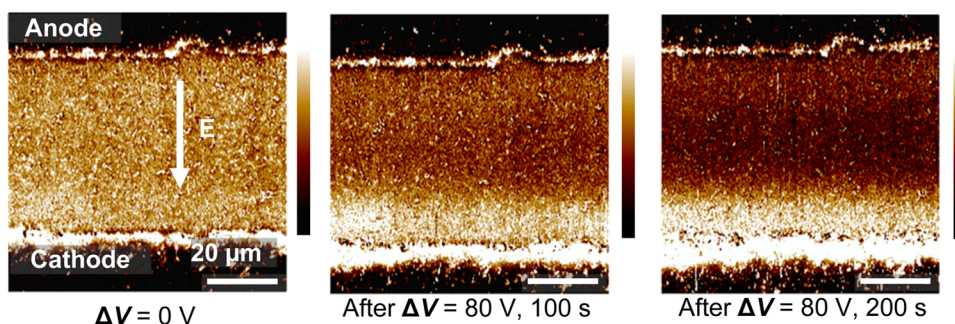


**Figure 32.** AFM-IR visualization of electromigration in a perovskite solar cell. Images show AFM-IR absorption at  $1468\text{ cm}^{-1}$ , corresponding to the  $\text{CH}_3$  antisymmetric stretching of the methylammonium ion. (left) Before application of a voltage across the anode/cathode; (center) after 80 V at 100 s; (right) after 80 V, 200 s. Note the increasing concentration of the methylammonium ion near the cathode after the voltage bias was applied. Adapted with permission from ref 116. Copyright 2015 John Wiley and Sons.



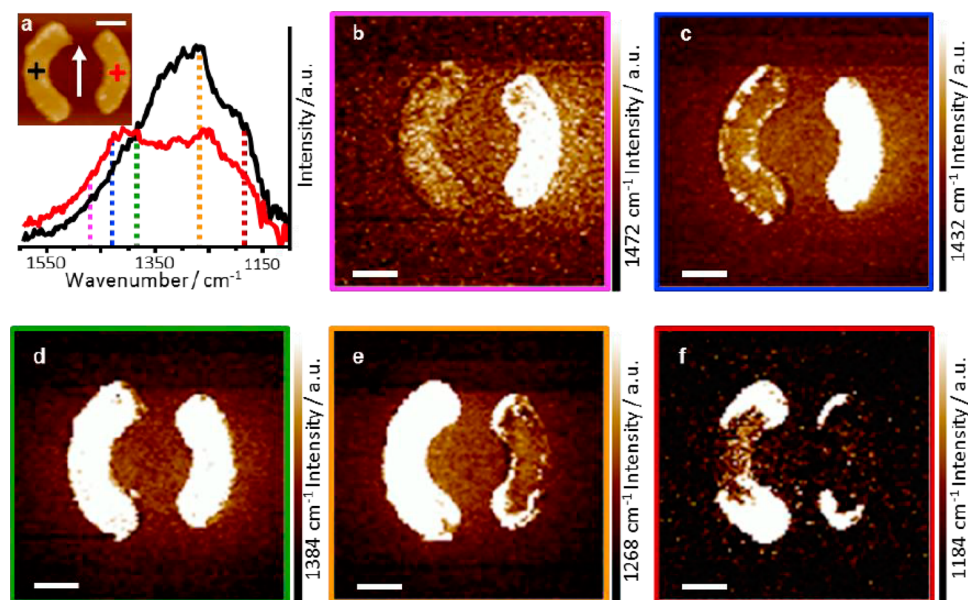


**Figure 33.** (a) AFM-IR spectrum and (b–f) AFM-IR absorption images taken on split ring resonators designed for surface-enhanced infrared absorption (SEIRA) applications. All scale bars are 500 nm, and the white arrow in (a) indicates the direction of the electric field of the incident radiation. Reprinted with permission from ref 119. Copyright 2014 John Wiley and Sons.

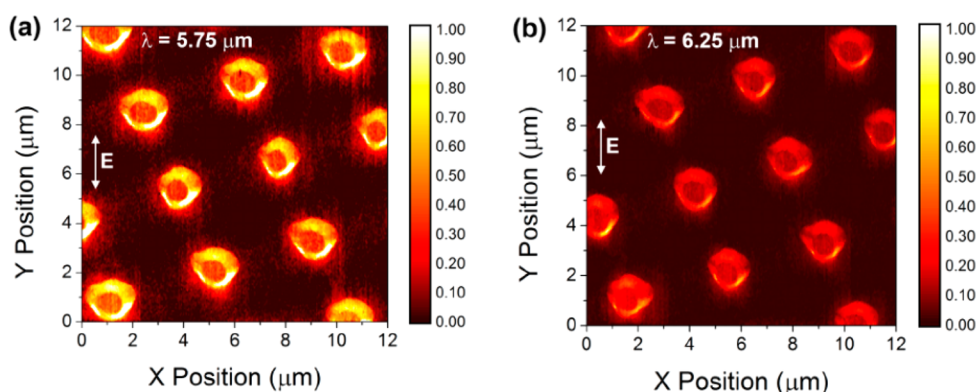


**Figure 34.** AFM-IR investigation of local surface plasmon resonances in InAs micropillars. The images show AFM-IR intensity maps at two different wavelengths, (a) 5.75  $\mu\text{m}$  and (b) 6.25. The arrow indicates the direction of the incident E-field. Reprinted from ref 118. Copyright 2013 AIP Publishing.

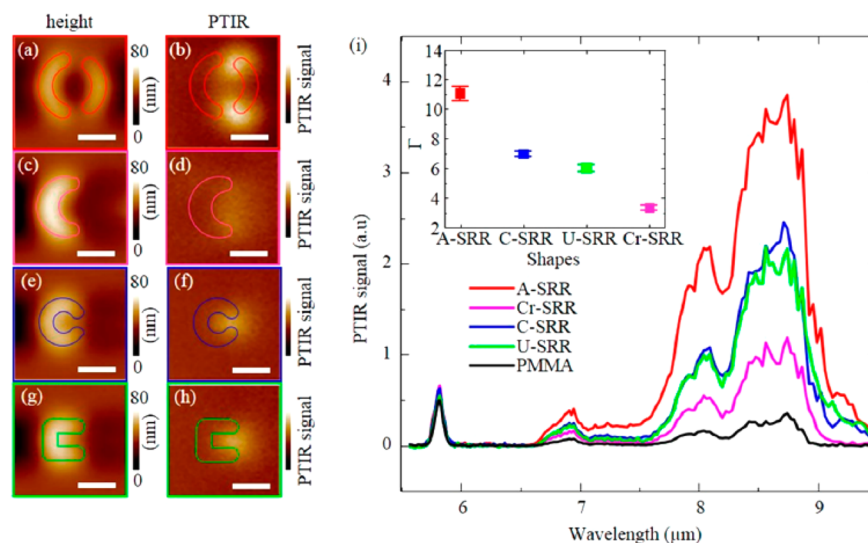
These nanostructures are designed to exhibit resonances at specific target wavelengths and hence enhance the strength of the incident radiation at the resonant wavelengths. Figure 33 shows measurements on the example SEIRA substrates measured by the Centrone group, including the pattern of dissipation within the plasmonics resonators at different wavelengths. The NIST group has also measured samples coated with thin layers of PMMA to visualize the field enhancement outside the bounds of the metallic plasmonic structures.<sup>120,122</sup>

AFM-IR has also been used to investigate localized surface plasmon resonances in InAs micropillars.<sup>118</sup> These structures have been studied by far field techniques, but both the structures and the distribution of the plasmonic enhancement have features that are well below the diffraction limit of conventional IR microspectroscopy. As such, conventional techniques can only provide far-field measurements of the spatially averaged enhancement. AFM-IR, however, can provide spatial resolution to the nanometer scale and hence provides a window to examine these structures and the enhancement/

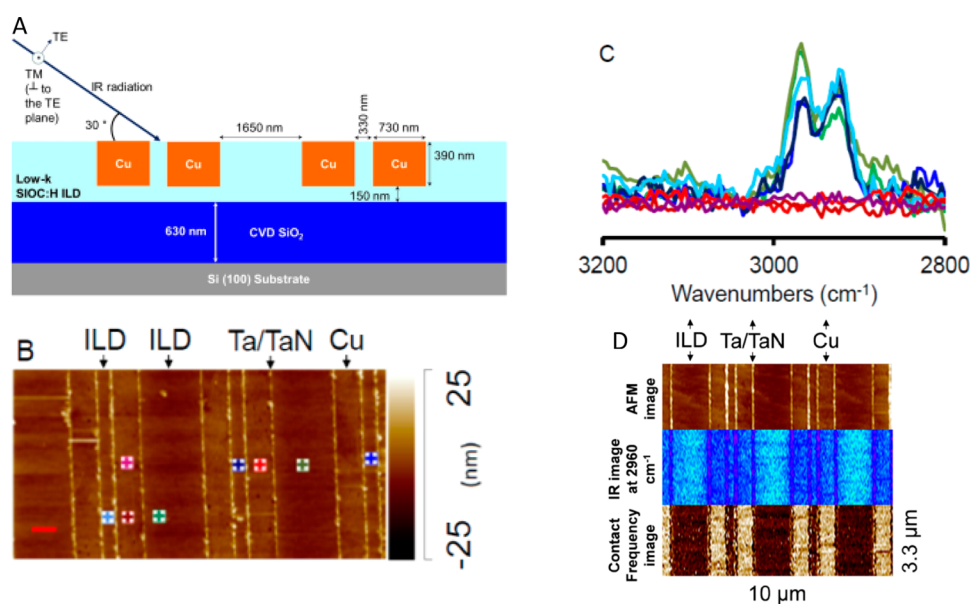
dissipation patterns on length scales that are well below the diffraction limit of conventional IR microspectroscopy.

Figure 34 shows examples of AFM-IR maps of InAs micropillars excited at different wavelengths. When excited at a resonant wavelength Ohmic heating of the semiconducting pillars results in a detectable thermal expansion signal.

While the previously mentioned publications measured the ohmic dissipation within conducting portions of plasmonics structure, it is also possible to use AFM-IR to visualize local field enhancements created by the plasmonic structures. Because the absorption enhancement is proportional to the local electric field, such AFM-IR maps enable one to qualitatively visualize the electric field extending outside the resonators. The Centrone group at NIST have applied thin polymer films on top of plasmonics resonators to act as a local “reporter” of the electric field distribution.<sup>120,122</sup> When the plasmonic resonant structure is excited by the IR light, the local electric field is strongly enhanced in specific locations in the structure proximity, leading to a local increase in the amount of IR energy absorbed by the polymer coating. Because the AFM-IR



**Figure 35.** AFM images (a, c, e, and g) and AFM-IR absorption images (b, d, f, and h) of various configurations of plasmonic resonators coated with a thin film of PMMA. The AFM-IR images show the extent and amount of field enhancement provided by the resonators when illuminated at  $8.75\ \mu\text{m}$ . Response spectra for various resonators are shown in (i). The inset in (i) quantifies the amount of field enhancement for different resonator configurations. (See ref 120 for details of resonator configurations.) Reprinted from ref 120. Copyright 2016 American Chemical Society.



**Figure 36.** Nanochemical and nanomechanical investigations of a semiconductor device including copper conductors, low-k interlayer dielectric (ILD) films, and Ta/TaN barrier films. (A) Schematic diagram of a cross section of the structure. (B) AFM topographic image of the top surface of the device. (C) AFM-IR spectra collected at different regions of the sample. Note the colors of the spectra correspond to the colors of the markers in (B) and reveal spectroscopic differences between the narrow and wide ILD lines. (D) Complementary correlative measurements of topography (top), IR absorption (middle), and stiffness (bottom, via contact resonance frequency measurement.) Reproduced by permission of from ref 126. Copyright 2016 The Electrochemical Society.

signal is proportional to the local absorbed energy, the stronger thermal expansion signal (with respect to bare polymer) detected by the AFM in correspondence to the absorption hotspots can be used to quantify the local electric field enhancement provided by the resonant structure. Figure 35 shows AFM images and corresponding AFM-IR absorption images and absorption spectra of various configurations of resonators coated with a thin layer of PMMA. Because the measurements in Figures 31–33 map the dissipation or local field enhancements on scales well below conventional optical resolution limits, these measurements can provide critical

insights into the performance and optimization of plasmonic structures.

**3.3.3. AFM-IR in Semiconductors.** AFM-IR has also been used for applications in the semiconductor field, measurements of quantum dots,<sup>124,125</sup> plasmonic semiconducting micro-particles,<sup>118</sup> GaAs phonon absorption, and mid-IR absorption of thin  $\text{SiO}_2$  microdisks,<sup>117</sup> as well as the in situ analysis of materials for interlayer dielectrics in semiconductor electronic devices.<sup>126</sup> Figure 36 shows example AFM-IR measurements on the surface of nanoelectronic contacts in a patterned semiconductor device, including Cu damascene conductors surrounded by an insulating low-k  $\text{SiOC:H}$  dielectric.<sup>126</sup> The

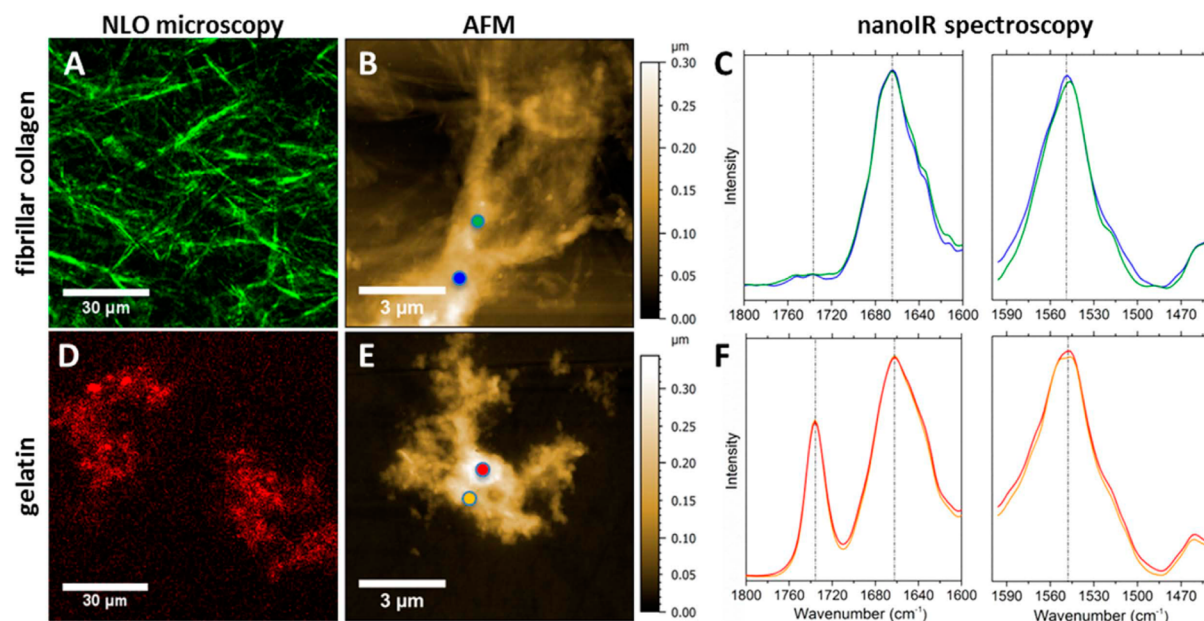


**Figure 37.** Nonlinear optical microscopy, AFM topography, and AFM-IR spectroscopic measurements of fibrillar collagen and gelatin samples. (A) Second harmonic generation optical microscopy highlights fibrils of collagen. (B) AFM topography image of fibrillar collagen sample with markers showing where (C) AFM-IR spectra were obtained. These AFM-IR spectra show expected amide I and II bands associated with the collagen protein. (D) Two photon fluorescence highlighting concentration of gelatin. (E) AFM image of gelatin sample showing markers where (F) AFM-IR spectra were obtained. The AFM-IR spectra show an additional peak at  $1725\text{ cm}^{-1}$  that is not present in the collagen sample. As such, this absorption peak can serve as an indicator for the presence of gelatinized regions in parchment samples. Reprinted with permission from ref 127. Copyright 2016 Nature Publishing Group.

study included nanoscale chemical analysis by AFM-IR as well as complementary nanomechanical analysis. Interestingly, this investigation revealed differences in the chemical composition of the SiOC:H dielectric material on the width and thickness of the patterned dielectric line. Specifically, AFM-IR measurements in Figure 36C revealed differing band ratios between the antisymmetric methyl stretching band at  $2968\text{ cm}^{-1}$  versus the antisymmetric methylene stretching band at  $2924\text{ cm}^{-1}$ . Similar spectral differences were also reproducibly observed in other regions of the spectrum. The study also performed correlative measurements of the chemical composition via AFM-IR absorbance imaging with  $2960\text{ cm}^{-1}$  laser excitation and measurements of the local stiffness via contact resonance AFM techniques using Lorentz Contact Resonance AFM.<sup>130</sup>

**3.3.4. AFM-IR in Cultural Heritage.** Another very promising application for AFM-IR is the field of cultural heritage, specifically the chemical analysis of historic artworks. There is intense interest within this community to understand the chemical details of materials used in specific works of art and to best understand mechanisms of degradation with the goal of better preservation and restoration. Gelatinization is a term commonly used for parchment degradation, and it refers to denaturation of collagen into gelatin, where the triple helix is dissociated. Unfortunately, little is known about the actual transformation process in parchments and the factors that influence it. AFM-IR and complementary optical techniques are providing new tools to study this denaturation process at the micro- and nanoscale. IR spectroscopy is used to examine collagen secondary structure in parchment and can be used to provide evidence of gelatinization.<sup>127</sup> However, the degradation process and the scale of fibrils ( $\sim 100\text{ nm}$ ) are below the diffraction limit of conventional IR microspectroscopy. AFM-IR, on the other hand, can be performed on individual fibrils to map the degradation process on relevant length scales. In

addition to the ability to perform nanoscale chemical analysis, AFM-IR has a specific advantage for cultural heritage applications as it requires only extremely small amounts of materials for analysis, a big advantage for irreplaceable pieces of art.

In this light, G. Latour et al.<sup>127</sup> have used the AFM-IR technique combined with nonlinear optical microscopy (NLO) to characterize the degradation of an historical parchment. Parchment is manufactured from animal skin and contains mainly fibrillar collagen (type I). For these experiments, several types of samples were studied, including untanned skin, a parchment sample of unknown origin, and actual fragments of a 17th century parchment marine map. As a control, reference samples of pure fibrillar collagen and gelatin were also prepared, representing the degraded state of collagen. All samples were studied using the AFM-IR technique and complementary nonlinear optical techniques, including the second harmonic generation and two-photon fluorescence.

Figure 37 shows nonlinear optical analysis and AFM-IR spectra of the reference samples of fibrillar collagen and gelatin samples. The fibrillar collagen spectra possess an amide I band characteristic of the protein carbonyl vibration and an associated amide II band due mainly to bending of the N–H bond. The spectra of the reference gelatin sample show an additional carbonyl absorption band around  $1740\text{ cm}^{-1}$ . This band can thus act as a marker for the gelatinization of collagen in actual parchment samples. As a test of this, a portion of a parchment sample was intentionally gelatinized through immersion in water. AFM-IR measurements detected a similar band ( $\sim 1725\text{ cm}^{-1}$ ) on the intentionally degraded parchment sample. These carbonyl bands in the  $1700\text{--}1750\text{ cm}^{-1}$  range seem to be related to the degradation of the fibrillar structure of collagen and probably linked to the many different processes like acidification, hydrolysis, and oxidation (Figure 38).



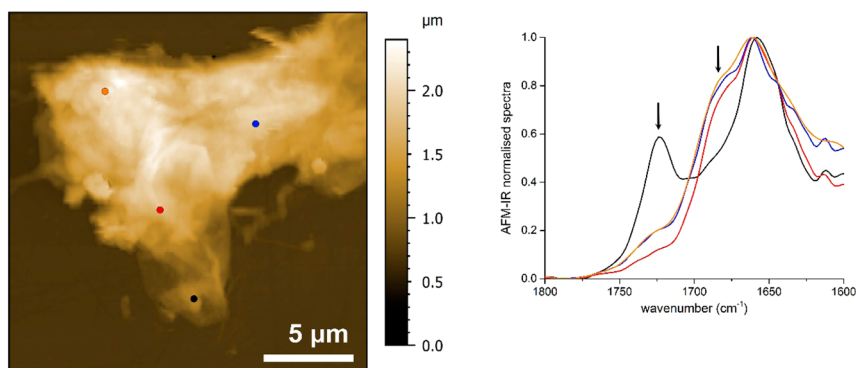


**Figure 38.** AFM-IR spectra of intentionally degraded parchment. (Right) AFM topography of a tiny thin scrap where the color spots indicate the location of spectra. (Left) AFM-IR spectra of the amide I region showing bands around 1700 and 1725  $\text{cm}^{-1}$  related to the denaturation of the fibrillar collagen structure. Reprinted with permission from ref 127. Copyright 2016 Nature Publishing Group.

Nonlinear optical microscopy (NLO), also called multiphoton microscopy, has also been previously applied in cultural heritage applications.<sup>131–133</sup> In this work, two NLO techniques were applied, second harmonic generation (SHG) and two-photon fluorescence. As shown in Figure 37, fibrillar collagen shows a SHG signature while gelatin shows a two-photon fluorescence signal. Thus, the degradation of collagen to gelatin can be tracked via the comparison of these two NLO signals.<sup>134,135</sup>

Next, a tiny scrap from a 17th century maritime map was studied by both AFM-IR and NLO techniques (Figure 39). The two-photon fluorescence image highlights regions of gelatinization. By imaging the sample with AFM-IR at the

carbonyl band previously associated with gelatinization (in this case at 1724  $\text{cm}^{-1}$ ), the researchers were able to map the distribution of gelatin formation with very high spatial resolution, far beyond the limits of conventional IR microspectroscopy. And in addition to the NLO techniques, the AFM-IR spectra provide rich potential for analysis of the detailed chemical nature, for example, via the exact position of the carbonyl band and the secondary structure based on the analysis of the amide I band contour. This study, combining nonlinear optical microscopy and nanoscale infrared spectroscopy and imaging, is an excellent example of the richness that correlated analysis of complementary techniques can bring. Moreover, the ability of the AFM-IR to chemically characterize a very small amount of sample, is also attractive and makes this technique a powerful tool for the analysis of museum artifacts.

#### 4. CONCLUSION

AFM-IR has emerged as a compelling new technique for providing chemical analysis and compositional mapping with nanoscale spatial resolution. It has overcome major limitations of the two techniques that it descends from. AFM-IR has overcome a key limitation of prior AFM techniques, specifically the lack of broadly applicable chemical analysis capability. AFM-IR has also overcome a fundamental limit of conventional infrared spectroscopy, specifically the spatial resolution limits imposed by diffraction. Combining nanoscale spatial resolution of AFM and the chemical analysis power of infrared spectroscopy, AFM-IR is rapidly finding utility and application in many diverse research areas in materials and life sciences and in academia and industry.

#### ASSOCIATED CONTENT

##### Supporting Information

The Supporting Information is available free of charge on the ACS Publications website at DOI: 10.1021/acs.chemrev.6b00448.

Theory description of AFM-IR operation, including optical absorption, photothermal expansion, the resulting motion of the AFM cantilever resulting from the absorbed radiation, comparison with different laser excitations, and general expression of resonance mode amplitude (PDF)

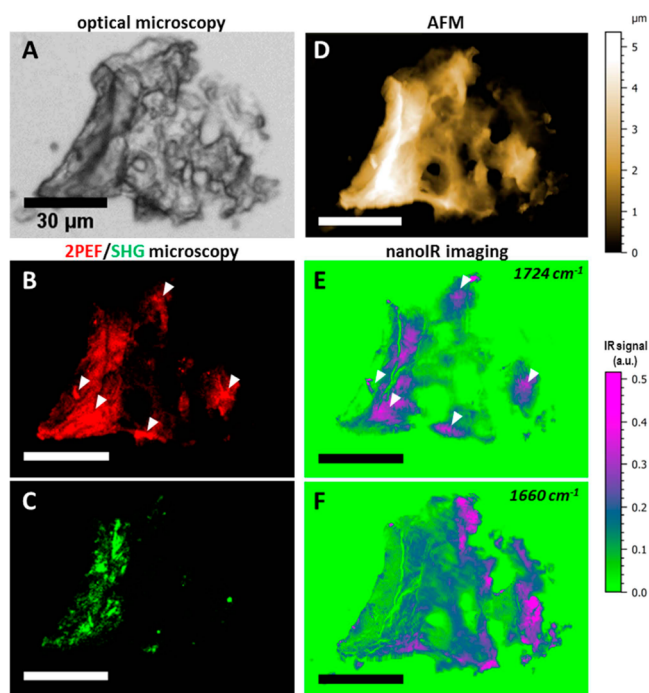


**Figure 39.** (A) Correlative optical microscope, (B) two photon excitation fluorescence (2PEF) microscopy, (C) SHG microscopy, (D) AFM topography, AFM-IR map at (E) 1724  $\text{cm}^{-1}$  and (F) 1660  $\text{cm}^{-1}$  from a 17th century maritime map sample. Arrows in the 2PEF microscopy image (B) show the hot fluorescent areas in the cluster and are correlated with the AFM-IR signal at 1724  $\text{cm}^{-1}$ . Reprinted with permission from ref 127. Copyright 2016 Nature Publishing Group.

## AUTHOR INFORMATION

## Corresponding Author

\*E-mail: alexandre.dazzi@u-psud.fr.

## Notes

The authors declare the following competing financial interest(s): Craig Prater is employed by Anasys Instruments, a manufacturer of instrumentation for AFM-based infrared spectroscopy. Alexandre Dazzi is a coinventor of AFM-IR patents licensed to Anasys Instruments.

## Biographies

Alexandre Dazzi is a tenured Professor of physics at Université Paris-Sud and works in the Laboratoire de Chimie Physique. Alexandre does research focused on the infrared domain and teaches Nanoscience at the Université Paris-Sud. He has a physics background with a focus on optics and near-field techniques. He has an undergraduate degree in material science and obtained his Ph.D. in 1998 at the Université de Bourgogne. In 2000, Alexandre took an associate professor position at the CLIO FEL facility, where he worked on near-field techniques in the infrared. After developing the AFM-IR technique, Alexander has worked to improved AFM-IR instrumentation and has focused heavily on the study of biomolecule production by microorganisms. Alexandre has also developed and supported AFM-IR user facilities.

Craig B. Prater is the Chief Technology Officer of Anasys Instruments. Craig received Ph.D. in physics from the University of California, Santa Barbara, in 1992 and has worked in the field of AFM-based scientific instrumentation for almost 30 years. Craig worked in various roles at Digital Instruments/Veeco Metrology from 1992–2007 and joined Anasys at CTO in 2007. Since joining Anasys, Craig has focused on developing technologies and instrumentation for nanoscale materials characterization, including nanoscale infrared spectroscopy and nanoscale mechanical spectroscopy.

## ACKNOWLEDGMENTS

The authors would like to thank and acknowledge Curtis Marcott, Kevin Kjoller, Will Bellomy, Lynne Taylor, and workers, A. Deniset-Besseau, J. Saunier, G. Latour, F. Lambert for their assistance. C.P. would like to thank the National Science Foundation and the Department of Energy for support of some of the work described herein. A.D. would like to thank the Université Paris-Sud through the ERM2011 grant for funding support.

## REFERENCES

- (1) Dazzi, A.; Prazeres, R.; Glotin, F.; Ortega, J. M. Local Infrared Microspectroscopy with Subwavelength Spatial Resolution with an Atomic Force Microscope Tip Used as a Photothermal Sensor. *Opt. Lett.* **2005**, *30* (18), 2388–2390.
- (2) Dazzi, A.; Prazeres, R.; Glotin, F.; Ortega, J. Subwavelength Infrared Spectromicroscopy Using an Afm as a Local Absorption Sensor. *Infrared Phys. Technol.* **2006**, *49* (1–2), 113–121.
- (3) Dazzi, A. Sub-100-Nanometer Infrared Spectroscopy and Imaging Based on a near-Field Photothermal Technique (PTIR). In *Biomedical Vibrational Spectroscopy*; Kneipp, J., Lasch, P., Eds. Wiley: Hoboken, NJ, 2008; pp 291–312.
- (4) Dazzi, A.; Prater, C. B.; Hu, Q.; Chase, D. B.; Rabolt, J. F.; Marcott, C. AFM-IR: Combining Atomic Force Microscopy and Infrared Spectroscopy for Nanoscale Chemical Characterization. *Appl. Spectrosc.* **2012**, *66* (12), 1365–1384.
- (5) Centrone, A. Infrared Imaging and Spectroscopy Beyond the Diffraction Limit. *Annu. Rev. Anal. Chem.* **2015**, *8*, 101–126.
- (6) Lasch, P.; Naumann, D. Spatial Resolution in Infrared Microspectroscopic Imaging of Tissues. *Biochim. Biophys. Acta, Biomembr.* **2006**, *1758* (7), 814–829.
- (7) Mattson, E. C.; Unger, M.; Clede, S.; Lambert, F.; Policar, C.; Imtiaz, A.; D'Souza, R.; Hirschmugl, C. J. Toward Optimal Spatial and Spectral Quality in Widefield Infrared Spectromicroscopy of Ir Labelled Single Cells. *Analyst* **2013**, *138* (19), 5610–5618.
- (8) Nasse, M. J.; Walsh, M. J.; Mattson, E. C.; Reininger, R.; Kajdacsy-Balla, A.; Macias, V.; Bhargava, R.; Hirschmugl, C. J. High-Resolution Fourier-Transform Infrared Chemical Imaging with Multiple Synchrotron Beams. *Nat. Methods* **2011**, *8* (5), 413–416.
- (9) Reddy, R. K.; Walsh, M. J.; Schulmerich, M. V.; Carney, P. S.; Bhargava, R. High-Definition Infrared Spectroscopic Imaging. *Appl. Spectrosc.* **2013**, *67* (1), 93–105.
- (10) Findlay, C. R.; Wiens, R.; Rak, M.; Sedlmair, J.; Hirschmugl, C. J.; Morrison, J.; Mundy, C. J.; Kansiz, M.; Gough, K. M. Rapid Bidiagnostic Ex Vivo Imaging at 1 Mm Pixel Resolution with Thermal Source Ftir Fpa. *Analyst* **2015**, *140* (7), 2493–2503.
- (11) Sarid, D. *Scanning Force Microscopy: With Applications to Electric, Magnetic, and Atomic Forces*; Oxford University Press on Demand: New York, 1994; Vol. 5.
- (12) Wilson, L.; Matsudaira, P. T.; Jena, B. P.; Horber, J. H. *Atomic Force Microscopy in Cell Biology*; Academic Press: San Diego, 2002; Vol. 68.
- (13) Drelich, J.; Mittal, K. L. *Atomic Force Microscopy in Adhesion Studies*; CRC Press: Leiden, 2005.
- (14) Eaton, P.; West, P. *Atomic Force Microscopy*; Oxford University Press: New York, 2010.
- (15) Haugstad, G. Probing Material Properties I: Phase Imaging. In *Atomic Force Microscopy*; John Wiley & Sons, Inc.: Hoboken, NJ, 2012; pp 187–257.
- (16) Haugstad, G. Probing Material Properties II: Adhesive Nanomechanics and Mapping Distance-Dependent Interactions. In *Atomic Force Microscopy*; John Wiley & Sons, Inc.: Hoboken, NJ, 2012; pp 258–329.
- (17) Haugstad, G., Probing Material Properties III: Lateral Force Methods. In *Atomic Force Microscopy*; John Wiley & Sons, Inc.: Hoboken, NJ, 2012; pp 330–378.
- (18) Hammiche, A.; Pollock, H. M.; Reading, M.; Claybourn, M.; Turner, P. H.; Jewkes, K. Photothermal Ft-Ir Spectroscopy: A Step Towards Ft-Ir Microscopy at a Resolution Better Than the Diffraction Limit. *Appl. Spectrosc.* **1999**, *53* (7), 810–815.
- (19) Anderson, M. S. Infrared Spectroscopy with an Atomic Force Microscope. *Appl. Spectrosc.* **2000**, *54* (3), 349–352.
- (20) Vodopyanov, K. L.; Schunemann, P. G. Broadly Tunable Noncritically Phase-Matched Znp<sub>2</sub> Optical Parametric Oscillator with a 2-Mj Pump Threshold. *Opt. Lett.* **2003**, *28*, 441–443.
- (21) Vodopyanov, K.; Hill, G.; Rice, J.; Meech, S.; Craig, D.; M Reading, M.; Dazzi, A.; Kjoller, K.; Prater, C. Nano-Spectroscopy in the 2.5–10 Micron Wavelength Range Using Atomic Force Microscope; *Frontiers in Optics 2009/Laser Science XXV/Fall 2009 OSA Optics & Photonics Technical Digest, OSA Technical Digest (CD)*; Optical Society of America: San Jose, California, 2009; p FMK2.
- (22) Lu, F.; Belkin, M. A. Infrared Absorption Nano-Spectroscopy Using Sample Photoexpansion Induced by Tunable Quantum Cascade Lasers. *Opt. Express* **2011**, *19*, 19942–19947.
- (23) Lu, F.; Jin, M.; Belkin, M. A. Tip-Enhanced Infrared Nanospectroscopy Via Molecular Expansion Force Detection. *Nat. Photonics* **2014**, *8* (4), 307–312.
- (24) Katzenmeyer, A. M.; Holland, G.; Kjoller, K.; Centrone, A. Absorption Spectroscopy and Imaging from the Visible through Mid-Infrared with 20 Nm Resolution. *Anal. Chem.* **2015**, *87* (6), 3154–3159.
- (25) Rabe, U.; Arnold, W. Acoustic Microscopy by Atomic Force Microscopy. *Appl. Phys. Lett.* **1994**, *64* (12), 1493–1493.
- (26) Rabe, U.; Janser, K.; Arnold, W. Vibrations of Free and Surface-Coupled Atomic Force Microscope Cantilevers: Theory and Experiment. *Rev. Sci. Instrum.* **1996**, *67* (9), 3281–3281.

- (27) Yamanaka, K.; Nakano, S. Quantitative Elasticity Evaluation by Contact Resonance in an Atomic Force Microscope. *Appl. Phys. A: Mater. Sci. Process.* **1998**, *66* (0), S313–S317.
- (28) Yamanaka, K.; Noguchi, A.; Tsuji, T.; Koike, T.; Goto, T. Quantitative Material Characterization by Ultrasonic Afm. *Surf. Interface Anal.* **1999**, *27* (5–6), 600–606.
- (29) Rabe, U.; Amelio, S.; Kester, E.; Scherer, V.; Hirsekorn, S.; Arnold, W. Quantitative Determination of Contact Stiffness Using Atomic Force Acoustic Microscopy. *Ultrasonics* **2000**, *38* (1–8), 430–437.
- (30) Yamanaka, K.; Maruyama, Y.; Tsuji, T.; Nakamoto, K. Resonance Frequency and Q Factor Mapping by Ultrasonic Atomic Force Microscopy. *Appl. Phys. Lett.* **2001**, *78* (13), 1939–1941.
- (31) Rabe, U.; Kopycinska, M.; Hirsekorn, S.; Arnold, W. Evaluation of the Contact Resonance Frequencies in Atomic Force Microscopy as a Method for Surface Characterisation (Invited). *Ultrasonics* **2002**, *40* (1–8), 49–54.
- (32) Rabe, U. Atomic Force Acoustic Microscopy. In *Applied Scanning Probe Methods II*, Bhushan, B., Fuchs, H., Eds. Springer: Berlin, 2006; pp 37–90.
- (33) Dazzi, A.; Glotin, F.; Carminati, R. Theory of Infrared Nanospectroscopy by Photothermal Induced Resonance. *J. Appl. Phys.* **2010**, *107*, 124519.
- (34) Lahiri, B.; Holland, G.; Centrone, A. Chemical Imaging Beyond the Diffraction Limit: Experimental Validation of the PTIR Technique. *Small* **2013**, *9*, 439–445.
- (35) Katzenmeyer, A. M.; Aksyuk, V.; Centrone, A. Nanoscale Infrared Spectroscopy: Improving the Spectral Range of the Photothermal Induced Resonance Technique. *Anal. Chem.* **2013**, *85* (4), 1972–1979.
- (36) Cho, H.; Felts, J. R.; Yu, M. F.; Bergman, L. A.; Vakakis, A. F.; King, W. P. Improved Atomic Force Microscope Infrared Spectroscopy for Rapid Nanometer-Scale Chemical Identification. *Nanotechnology* **2013**, *24* (44), 444007.
- (37) Katzenmeyer, A. M.; Holland, G.; Chae, J.; Band, A.; Kjoller, K.; Centrone, A. Mid-Infrared Spectroscopy Beyond the Diffraction Limit Via Direct Measurement of the Photothermal Effect. *Nanoscale* **2015**, *7* (42), 17637–17641.
- (38) Zenhausern, F.; O'Boyle, M. P.; Wickramasinghe, H. K. Apertureless near-Field Optical Microscope. *Appl. Phys. Lett.* **1994**, *65* (13), 1623–1625.
- (39) Anderson, M. S. Locally Enhanced Raman Spectroscopy with an Atomic Force Microscope. *Appl. Phys. Lett.* **2000**, *76* (21), 3130–3132.
- (40) Stöckle, R. M.; Suh, Y. D.; Deckert, V.; Zenobi, R. Nanoscale Chemical Analysis by Tip-Enhanced Raman Spectroscopy. *Chem. Phys. Lett.* **2000**, *318* (1–3), 131–136.
- (41) Hayazawa, N.; Inouye, Y.; Sekkat, Z.; Kawata, S. Metallized Tip Amplification of near-Field Raman Scattering. *Opt. Commun.* **2000**, *183* (1–4), 333–336.
- (42) Muller, E. A.; Pollard, B.; Raschke, M. B. Infrared Chemical Nano-Imaging: Accessing Structure, Coupling, and Dynamics on Molecular Length Scales. *J. Phys. Chem. Lett.* **2015**, *6* (7), 1275–1284.
- (43) Pettinger, B.; Schambach, P.; Villagómez, C. J.; Scott, N. Tip-Enhanced Raman Spectroscopy: Near-Fields Acting on a Few Molecules. *Annu. Rev. Phys. Chem.* **2012**, *63* (1), 379–399.
- (44) Kumar, N.; Mignuzzi, S.; Su, W.; Roy, D. Tip-Enhanced Raman Spectroscopy: Principles and Applications. *EPJ Techniques and Instrumentation* **2015**, *2* (1), 1–23.
- (45) Sonntag, M. D.; Pozzi, E. A.; Jiang, N.; Hersam, M. C.; Van Duyne, R. P. Recent Advances in Tip-Enhanced Raman Spectroscopy. *J. Phys. Chem. Lett.* **2014**, *5* (18), 3125–3130.
- (46) Govyadinov, A. A.; Amenabar, I.; Huth, F.; Carney, P. S.; Hillenbrand, R. Quantitative Measurement of Local Infrared Absorption and Dielectric Function with Tip-Enhanced near-Field Microscopy. *J. Phys. Chem. Lett.* **2013**, *4* (9), 1526–1531.
- (47) Mastel, S.; Govyadinov, A. A.; de Oliveira, T. V. A. G.; Amenabar, I.; Hillenbrand, R. Nanoscale-Resolved Chemical Identification of Thin Organic Films Using Infrared near-Field Spectroscopy and Standard Fourier Transform Infrared References. *Appl. Phys. Lett.* **2015**, *106* (2), 023113.
- (48) Marcott, C.; Lo, M.; Kjoller, K.; Prater, C.; Noda, I. Spatial Differentiation of Sub-Micrometer Domains in a Poly (Hydroxyalkanoate) Copolymer Using Instrumentation That Combines Atomic Force Microscopy (Afm) and Infrared (Ir) Spectroscopy. *Appl. Spectrosc.* **2011**, *65* (10), 1145–1150.
- (49) Ye, J.; Midorikawa, H.; Awatani, T.; Marcott, C.; Lo, M.; Kjoller, K.; Shetty, R. Nanoscale Infrared Spectroscopy and AFM Imaging of a Polycarbonate/Acrylonitrile-Styrene/Butadiene Blend. *Microscopy and Analysis* **2012**, April, 24–27.
- (50) Tang, F.; Bao, P.; Su, Z. Analysis of Nanodomain Composition in High-Impact Polypropylene by Atomic Force Microscopy-Infrared. *Anal. Chem.* **2016**, *88* (9), 4926–4930.
- (51) Brown, P. S.; Bhushan, B. Durable, Superoleophobic Polymer–Nanoparticle Composite Surfaces with Re-Entrant Geometry Via Solvent-Induced Phase Transformation. *Sci. Rep.* **2016**, *6*, 21048.
- (52) Eby, T.; Gundusharma, U.; Lo, M.; Sahagian, K.; Marcott, C.; Kjoller, K. Reverse Engineering of Polymeric Multilayers Using AFM-Based Nanoscale Ir Spectroscopy and Thermal Analysis. *Spectrosc. Eur.* **2012**, *24* (3), 18–21.
- (53) Felts, J. R.; Kjoller, K.; Lo, M.; Prater, C. B.; King, W. P. Nanometer-Scale Infrared Spectroscopy of Heterogeneous Polymer Nanostructures Fabricated by Tip-Based Nanofabrication. *ACS Nano* **2012**, *6* (9), 8015–8021.
- (54) Felts, J. R.; Cho, H.; Yu, M.-F.; Bergman, L. A.; Vakakis, A. F.; King, W. P. Atomic Force Microscope Infrared Spectroscopy on 15 Nm Scale Polymer Nanostructures. *Rev. Sci. Instrum.* **2013**, *84* (2), No. 023709.
- (55) Gong, L.; Chase, D. B.; Noda, I.; Liu, J.; Martin, D. C.; Ni, C.; Rabolt, J. F. Discovery of B-Form Crystal Structure in Electrospun Poly[(R)-3-Hydroxybutyrate-Co-(R)-3-Hydroxyhexanoate] (Phbhx) Nanofibers: From Fiber Mats to Single Fibers. *Macromolecules* **2015**, *48* (17), 6197–6205.
- (56) Awatani, T.; Midorikawa, H.; Kojima, N.; Ye, J.; Marcott, C. Morphology of Water Transport Channels and Hydrophobic Clusters in Nafion from High Spatial Resolution Afm-Ir Spectroscopy and Imaging. *Electrochem. Commun.* **2013**, *30* (0), 5–8.
- (57) Van Eerdenbrugh, B.; Lo, M.; Kjoller, K.; Marcott, C.; Taylor, L. S. Nanoscale Mid-Infrared Evaluation of the Miscibility Behavior of Blends of Dextran or Maltodextrin with Poly(Vinylpyrrolidone). *Mol. Pharmaceutics* **2012**, *9* (5), 1459–1469.
- (58) Van Eerdenbrugh, B.; Lo, M.; Kjoller, K.; Marcott, C.; Taylor, L. S. Nanoscale Mid-Infrared Imaging of Phase Separation in a Drug–Polymer Blend. *J. Pharm. Sci.* **2012**, *101* (6), 2066–2073.
- (59) Harrison, A. J.; Bilgili, E. A.; Beaudoin, S. P.; Taylor, L. S. Atomic Force Microscope Infrared Spectroscopy of Griseofulvin Nanocrystals. *Anal. Chem.* **2013**, *85* (23), 11449–11455.
- (60) Li, N.; Taylor, L. S. Nanoscale Infrared, Thermal, and Mechanical Characterization of Telaprevir–Polymer Miscibility in Amorphous Solid Dispersions Prepared by Solvent Evaporation. *Mol. Pharmaceutics* **2016**, *13* (3), 1123–1136.
- (61) Purohit, H. S.; Taylor, L. S. Miscibility of Itraconazole–Hydroxypropyl Methylcellulose Blends: Insights with High Resolution Analytical Methodologies. *Mol. Pharmaceutics* **2015**, *12* (12), 4542–4553.
- (62) Kelchtermans, M.; Lo, M.; Dillon, E.; Kjoller, K.; Marcott, C. Characterization of a Polyethylene–Polyamide Multilayer Film Using Nanoscale Infrared Spectroscopy and Imaging. *Vib. Spectrosc.* **2016**, *82*, 10–15.
- (63) Lu, P.; Ding, B. Applications of Electrospun Fibers. *Recent Pat. Nanotechnol.* **2008**, *2* (3), 169–82.
- (64) Akyildiz, H. I.; Lo, M.; Dillon, E.; Roberts, A. T.; Everitt, H. O.; Jur, J. S. Formation of Novel Photoluminescent Hybrid Materials by Sequential Vapor Infiltration into Polyethylene Terephthalate Fibers. *J. Mater. Res.* **2014**, *29* (23), 2817–2826.
- (65) Ghosh, S.; Ramos, L.; Remita, S.; Dazzi, A.; Deniset-Besseau, A.; Beaunier, P.; Goubard, F.; Aubert, P.-H.; Remita, H. Conducting



Polymer Nanofibers with Controlled Diameters Synthesized in Hexagonal Mesophases. *New J. Chem.* **2015**, 39 (11), 8311–8320.

(66) Coletta, C.; Cui, Z.; Dazzi, A.; Guigner, J.-M.; Néron, S.; Marignier, J.-L.; Remita, S. A Pulsed Electron Beam Synthesis of Pedot Conducting Polymers by Using Sulfate Radicals as Oxidizing Species. *Radiat. Phys. Chem.* **2016**, 126, 21–31.

(67) Bandekar, J.; Sawyer, A. Ft-Ir Spectroscopic Studies of Polyurethanes: IV. Studies of the Effect of the Presence of Processing Aids on the Hemocompatibility of Polyurethanes. *J. Biomater. Sci., Polym. Ed.* **1996**, 7 (6), 485–501.

(68) Sawyer, A.; Bandekar, J.; Li, H. Examination of Wax on Surface of Extruded Pellethane by Scanning Electron Microscopy Attenuated Total Reflection-Infrared and X-Ray Photoelectron Spectroscopy and Its Importance in Blood Compatibility. *J. Vac. Sci. Technol., A* **1994**, 12 (5), 2966–2966.

(69) Duwez, A. S.; Poleunis, C.; Bertrand, P.; Nysten, B. Chemical Recognition of Antioxidants and Uv-Light Stabilizers at the Surface of Polypropylene: Atomic Force Microscopy with Chemically Modified Tips. *Langmuir* **2001**, 17 (20), 6351–6357.

(70) Médard, N.; Benninghoven, A.; Rading, D.; Licciardello, A.; Auditore, A.; Duc, T.; Min; Montigaud, H.; Vernerey, F.; Poleunis, C.; et al. Antioxidant Segregation and Crystallisation at Polyester Surfaces Studied by TOF-SIMS. *Appl. Surf. Sci.* **2003**, 203–204, 571–574.

(71) Médard, N.; Bertrand, P. Additive Behavior in Ultrathin Polymer Films Investigated by ToF-Sims. *Appl. Surf. Sci.* **2004**, 231–232, 309–313.

(72) Saunier, J.; Mazel, V.; Paris, C.; Yagoubi, N. Polymorphism of Irganox 1076®: Discovery of New Forms and Direct Characterization of the Polymorphs on a Medical Device by Raman Microspectroscopy. *Eur. J. Pharm. Biopharm.* **2010**, 75 (3), 443–450.

(73) Dazzi, A.; Saunier, J.; Kjoller, K.; Yagoubi, N. Resonance Enhanced AFM-IR: A New Powerful Way to Characterize Blooming on Polymers Used in Medical Devices. *Int. J. Pharm.* **2015**, 484 (1–2), 109–114.

(74) Baden, N.; Yasuda, M.; Yoshida, A.; Muraki, N. In *New Method for Chemical Characterization of Polymer Materials in Industrial Devices: AFM-IR with FIB Sample Preparation*; IEEE 22nd International Symposium on the Physical and Failure Analysis of Integrated Circuits, June 29–July 2, 2015; IEEE: Piscataway, NJ, 2015; pp 496–499.

(75) Morsch, S.; Lyon, S.; Greensmith, P.; Smith, S. D.; Gibbon, S. R. Mapping Water Uptake in Organic Coatings Using Afm-Ir. *Faraday Discuss.* **2015**, 180 (0), 527–542.

(76) Morsch, S.; Liu, Y.; Lyon, S. B.; Gibbon, S. R. Insights into Epoxy Network Nanostructural Heterogeneity Using Afm-Ir. *ACS Appl. Mater. Interfaces* **2016**, 8 (1), 959–966.

(77) Morsch, S.; Lyon, S.; Gibbon, S. R. The Degradation Mechanism of an Epoxy-Phenolic Can Coating. *Prog. Org. Coat.* **2016**, DOI: 10.1016/j.porgcoat.2016.03.019, in press.

(78) Baldassarre, L.; Giliberti, V.; Rosa, A.; Ortolani, M.; Bonamore, A.; Baiocco, P.; Kjoller, K.; Calvani, P.; Nucara, A. Mapping the Amide I Absorption in Single Bacteria and Mammalian Cells with Resonant Infrared Nanospectroscopy. *Nanotechnology* **2016**, 27 (7), 075101.

(79) Dazzi, A.; Prazeres, R.; Glotin, F.; Ortega, J. M.; Al-Sawaftah, M.; de Frutos, M. Chemical Mapping of the Distribution of Viruses into Infected Bacteria with a Photothermal Method. *Ultramicroscopy* **2008**, 108 (7), 635–41.

(80) Janik, E.; Bednarska, J.; Zubik, M.; Puzio, M.; Luchowski, R.; Grudzinski, W.; Mazur, R.; Garstka, M.; Maksymiec, W.; Kulik, A.; et al. Molecular Architecture of Plant Thylakoids under Physiological and Light Stress Conditions: A Study of Lipid–Light-Harvesting Complex Ii Model Membranes. *Plant Cell* **2013**, 25 (6), 2155–2170.

(81) Mayet, C.; Deniset-Besseau, A.; Prazeres, R.; Ortega, J.-M.; Dazzi, A. Analysis of Bacterial Polyhydroxybutyrate Production by Multimodal Nanoimaging. *Biotechnol. Adv.* **2013**, 31 (3), 369–374.

(82) Khanal, D.; Kondyurin, A.; Hau, H.; Knowles, J. C.; Levinson, O.; Ramzan, I.; Fu, D.; Marcott, C.; Chrzanowski, W. Biospectroscopy of Nanodiamond-Induced Alterations in Conformation of Intra- and

Extracellular Proteins – a Nanoscale IR Study. *Anal. Chem.* **2016**, 88 (15), 7530–7538.

(83) Gourion-Arsiquaud, S.; Marcott, C.; Hu, Q.; Boskey, A. Studying Variations in Bone Composition at Nano-Scale Resolution: A Preliminary Report. *Calcif. Tissue Int.* **2014**, 95 (5), 413–418.

(84) Muller, T.; Ruggeri, F. S.; Kulik, A. J.; Shimanovich, U.; Mason, T. O.; Knowles, T. P. J.; Dietler, G. Nanoscale Spatially Resolved Infrared Spectra from Single Microdroplets. *Lab Chip* **2014**, 14 (7), 1315–1319.

(85) Ruggeri, F. S.; Byrne, C.; Khemtemourian, L.; Ducouret, G.; Dietler, G.; Jacquot, Y. Concentration-Dependent and Surface-Assisted Self-Assembly Properties of a Bioactive Estrogen Receptor A-Derived Peptide. *J. Pept. Sci.* **2015**, 21 (2), 95–104.

(86) Ruggeri, F. S.; Longo, G.; Faggiano, S.; Lipiec, E.; Pastore, A.; Dietler, G. Infrared Nanospectroscopy Characterization of Oligomeric and Fibrillar Aggregates During Amyloid Formation. *Nat. Commun.* **2015**, 6, 7831–7831.

(87) Ruggeri, F. S.; Vieweg, S.; Cendrowska, U.; Longo, G.; Chiki, A.; Lashuel, H. A.; Dietler, G. Nanoscale Studies Link Amyloid Maturity with Polyglutamine Diseases Onset. *Sci. Rep.* **2016**, 6, 1–10.

(88) Hu, Q.; Sommerfeld, M.; Jarvis, E.; Ghirardi, M.; Posewitz, M.; Seibert, M.; Darzins, A. Microalgal Triacylglycerols as Feedstocks for Biofuel Production: Perspectives and Advances. *Plant J.* **2008**, 54 (4), 621–639.

(89) Atsumi, S.; Liao, J. C. Metabolic Engineering for Advanced Biofuels Production from Escherichia Coli. *Curr. Opin. Biotechnol.* **2008**, 19 (5), 414–419.

(90) Lu, X.; Vora, H.; Khosla, C. Overproduction of Free Fatty Acids in E. Coli: Implications for Biodiesel Production. *Metab. Eng.* **2008**, 10 (6), 333–339.

(91) Bokinsky, G.; Peralta-Yahya, P. P.; George, A.; Holmes, B. M.; Steen, E. J.; Dietrich, J.; Lee, T. S.; Tullman-Ercek, D.; Voigt, C. A.; Simmons, B. A.; et al. Synthesis of Three Advanced Biofuels from Ionic Liquid-Pretreated Switchgrass Using Engineered Escherichia Coli. *Proc. Natl. Acad. Sci. U. S. A.* **2011**, 108 (50), 19949–19954.

(92) Goodfellow, M.; W., S.T.; Mordarski, M. *Actinomyces in Biotechnology*; Elsevier: London, 1988.

(93) Butler, P. R.; Brown, M.; Oliver, S. G. Improvement of Antibiotic Titrers from Streptomyces Bacteria by Interactive Continuous Selection. *Biotechnol. Bioeng.* **1996**, 49 (2), 185–196.

(94) Hopwood, D. A. *Streptomyces in Nature and Medicine: The Antibiotic Markers*; Oxford University Press: New York, 2007.

(95) Fischer, C. R.; Klein-Marcuschamer, D.; Stephanopoulos, G. Selection and Optimization of Microbial Hosts for Biofuels Production. *Metab. Eng.* **2008**, 10 (6), 295–304.

(96) Arabolaza, A.; Rodriguez, E.; Altabe, S.; Alvarez, H.; Gramajo, H. Multiple Pathways for Triacylglycerol Biosynthesis in Streptomyces Coelicolor. *Appl. Environ. Microbiol.* **2008**, 74 (9), 2573–2582.

(97) Zhu, Q.; Jackson, E. N. Metabolic Engineering of Yarrowia Lipolytica for Industrial Applications. *Curr. Opin. Biotechnol.* **2015**, 36, 65–72.

(98) Dean, A. P.; Sigee, D. C.; Estrada, B.; Pittman, J. K. Using Ftir Spectroscopy for Rapid Determination of Lipid Accumulation in Response to Nitrogen Limitation in Freshwater Microalgae. *Bioresour. Technol.* **2010**, 101 (12), 4499–4507.

(99) Ami, D.; Poster, R.; Mereghetti, P.; Porro, D.; Doglia, S. M.; Branduardi, P. Fourier Transform Infrared Spectroscopy as a Method to Study Lipid Accumulation in Oleaginous Yeasts. *Biotechnol. Biofuels* **2014**, 7 (1), 12–12.

(100) Meng, Y.; Yao, C.; Xue, S.; Yang, H. Application of Fourier Transform Infrared (FT-IR) Spectroscopy in Determination of Microalgal Compositions. *Bioresour. Technol.* **2014**, 151, 347–354.

(101) Deniset-Besseau, A.; Prater, C. B.; Virolle, M.-J.; Dazzi, A. Monitoring Triacylglycerols Accumulation by Atomic Force Microscopy Based Infrared Spectroscopy in Streptomyces Species for Biodiesel Applications. *J. Phys. Chem. Lett.* **2014**, 5 (4), 654–658.

(102) Kuimova, M. K.; Chan, K. L. A.; Kazarian, S. G. Chemical Imaging of Live Cancer Cells in the Natural Aqueous Environment. *Appl. Spectrosc.* **2009**, 63 (2), 164–171.

- (103) Wetzel, D. L. Mid-Ir and near-IT Chemical Imaging: Complementary for Biological Materials. *Vib. Spectrosc.* **2012**, *60* (60), 29–33.
- (104) Kazarian, S. G.; Chan, K. L. A. ATR-FTIR Spectroscopic Imaging: Recent Advances and Applications to Biological Systems. *Analyst* **2013**, *138* (7), 1940–51.
- (105) Dumas, P.; Sockalingum, G. D.; Sulé-Suso, J. Adding Synchrotron Radiation to Infrared Microspectroscopy: What's New in Biomedical Applications? *Trends Biotechnol.* **2007**, *25* (1), 40–44.
- (106) Hirschmugl, C. J.; Gough, K. M. Fourier Transform Infrared Spectrochemical Imaging: Review of Design and Applications with a Focal Plane Array and Multiple Beam Synchrotron Radiation Source. *Appl. Spectrosc.* **2012**, *66*, 475–491.
- (107) Clède, S.; Policar, C.; Sandt, C. Fourier Transform Infrared (Ft-Ir) Spectromicroscopy to Identify Cell Organelles: Correlation with Fluorescence Staining in MCF-7 Breast Cancer Cells. *Appl. Spectrosc.* **2014**, *68* (1), 113–117.
- (108) Clède, S.; Lambert, F.; Sandt, C.; Kascakova, S.; Unger, M.; Harté, E.; Plamont, M. A.; Saint-Fort, R.; Deniset-Besseau, A.; Gueroui, Z.; Hirschmugl, C.; et al. Detection of an Estrogen Derivative in Two Breast Cancer Cell Lines Using a Single Core Multimodal Probe for Imaging (SCoMPI) Imaged by a Panel of Luminescent and Vibrational Techniques. *Analyst* **2013**, *138* (19), 5627–5638.
- (109) Policar, C.; Waern, J. B.; Plamont, M. A.; Clède, S.; Mayet, C.; Prazeres, R.; Ortega, J. M.; Vessièrès, A.; Dazzi, A. Subcellular Ir Imaging of a Metal-Carbonyl Moiety Using Photothermally Induced Resonance. *Angew. Chem., Int. Ed.* **2011**, *50*, 860–864.
- (110) Marcott, C.; Lo, M.; Kjoller, K.; Domanov, Y.; Balooch, G.; Luengo, G. S. Nanoscale Infrared (Ir) Spectroscopy and Imaging of Structural Lipids in Human Stratum Corneum Using an Atomic Force Microscope to Directly Detect Absorbed Light from a Tunable Ir Laser Source. *Exp. Dermatol.* **2013**, *22* (6), 419–21.
- (111) Marcott, C.; Lo, M.; Kjoller, K.; Fiat, F.; Baghdadli, N.; Balooch, G.; Luengo, G. S. Localization of Human Hair Structural Lipids Using Nanoscale Infrared Spectroscopy and Imaging. *Appl. Spectrosc.* **2014**, *68* (5), 564–569.
- (112) Fowler, D. M.; Koulov, A. V.; Balch, W. E.; Kelly, J. W. Functional Amyloid – from Bacteria to Humans. *Trends Biochem. Sci.* **2007**, *32* (5), 217–224.
- (113) Shewmaker, F.; McGlinchey, R. P.; Wickner, R. B. Structural Insights into Functional and Pathological Amyloid. *J. Biol. Chem.* **2011**, *286*, 16533–16540.
- (114) Katzenmeyer, A. M.; Canivet, J.; Holland, G.; Farrusseng, D.; Centrone, A. Assessing Chemical Heterogeneity at the Nanoscale in Mixed-Ligand Metal–Organic Frameworks with the Ptir Technique. *Angew. Chem., Int. Ed.* **2014**, *53* (11), 2852–2856.
- (115) Dong, R.; Fang, Y.; Chae, J.; Dai, J.; Xiao, Z.; Dong, Q.; Yuan, Y.; Centrone, A.; Zeng, X. C.; Huang, J. High-Gain and Low-Driving-Voltage Photodetectors Based on Organolead Triiodide Perovskites. *Adv. Mater.* **2015**, *27* (11), 1912–1918.
- (116) Yuan, Y.; Chae, J.; Shao, Y.; Wang, Q.; Xiao, Z.; Centrone, A.; Huang, J. Photovoltaic Switching Mechanism in Lateral Structure Hybrid Perovskite Solar Cells. *Adv. Energy Mater.* **2015**, *5* (15), 1500615.
- (117) Houel, J.; Homeyer, E.; Sauvage, S.; Boucaud, P.; Dazzi, A.; Prazeres, R.; Ortega, J. M. Midinfrared Absorption Measured at a Lambda/400 Resolution with an Atomic Force Microscope. *Opt. Express* **2009**, *17* (13), 10887–94.
- (118) Felts, J. R.; Law, S.; Roberts, C. M.; Podolskiy, V.; Wasserman, D. M.; King, W. P. Near-Field Infrared Absorption of Plasmonic Semiconductor Microparticles Studied Using Atomic Force Microscope Infrared Spectroscopy. *Appl. Phys. Lett.* **2013**, *102* (15), 152110–5.
- (119) Katzenmeyer, A. M.; Chae, J.; Kasic, R.; Holland, G.; Lahiri, B.; Centrone, A. Nanoscale Imaging and Spectroscopy of Plasmonic Modes with the Ptir Technique. *Adv. Opt. Mater.* **2014**, *2* (8), 718–722.
- (120) Chae, J.; Lahiri, B.; Centrone, A. Engineering near-Field Seira Enhancements in Plasmonic Resonators. *ACS Photonics* **2016**, *3* (1), 87–95.
- (121) Aksyuk, V.; Lahiri, B.; Holland, G.; Centrone, A. Near-Field Asymmetries in Plasmonic Resonators. *Nanoscale* **2015**, *7* (8), 3634–3644.
- (122) Lahiri, B.; Holland, G.; Aksyuk, V.; Centrone, A. Nanoscale Imaging of Plasmonic Hot Spots and Dark Modes with the Photothermal-Induced Resonance Technique. *Nano Lett.* **2013**, *13* (7), 3218–3224.
- (123) Chae, J.; Lahiri, B.; Kohoutek, J.; Holland, G.; Lezec, H.; Centrone, A. Metal-Dielectric-Metal Resonators with Deep Sub-wavelength Dielectric Layers Increase the near-Field Seira Enhancement. *Opt. Express* **2015**, *23* (20), 25912–25922.
- (124) Houel, J.; Sauvage, S.; Boucaud, P.; Dazzi, A.; Prazeres, R.; Glotin, F.; Ortéga, J.-M.; Miard, A.; Lemaître, A. Ultraweak-Absorption Microscopy of a Single Semiconductor Quantum Dot in the Midinfrared Range. *Phys. Rev. Lett.* **2007**, *99* (21), 217404.
- (125) Sauvage, S.; Driss, A.; Réveret, F.; Boucaud, P.; Dazzi, A.; Prazeres, R.; Glotin, F.; Ortéga, J.-M.; Miard, A.; Halioua, Y.; et al. Homogeneous Broadening of the S to P Transition in InGaAs/GaAs Quantum Dots Measured by Infrared Absorption Imaging with Nanoscale Resolution. *Phys. Rev. B: Condens. Matter Mater. Phys.* **2011**, *83* (3), 035302.
- (126) Lo, M. K. F.; Dazzi, A.; Marcott, C. A.; Dillon, E.; Hu, Q.; Kjoller, K.; Prater, C. B.; King, S. W. Nanoscale Chemical-Mechanical Characterization of Nanoelectronic Low-K Dielectric/Cu Interconnects. *ECS J. Solid State Sci. Technol.* **2016**, *5* (4), P3018–P3024.
- (127) Latour, G.; Robinet, L.; Dazzi, A.; Portier, F.; Deniset-Besseau, A.; Schanne-Klein, M.-C. Correlative Nonlinear Optical Microscopy and Infrared Nanoscopy Reveals Collagen Degradation in Altered Parchments. *Sci. Rep.* **2016**, *6*, 26344.
- (128) Collavini, S.; Völker, S. F.; Delgado, J. L. Understanding the Outstanding Power Conversion Efficiency of Perovskite-Based Solar Cells. *Angew. Chem., Int. Ed.* **2015**, *54* (34), 9757–9759.
- (129) NREL Best Research-Cell Efficiencies Chart (Rev Aug 12, 2016). [http://www.nrel.gov/ncpv/images/efficiency\\_chart.jpg](http://www.nrel.gov/ncpv/images/efficiency_chart.jpg) (accessed Oct 18, 2016).
- (130) Lee, B.; Prater, C. B.; King, W. P. Lorentz Force Actuation of a Heated Atomic Force Microscope Cantilever. *Nanotechnology* **2012**, *23*, 055709.
- (131) Cormack, I. G.; Loza-Alvarez, P.; Sarrado, L.; Tomás, S.; Amat-Roldan, I.; Torner, L.; Artigas, D.; Guitart, J.; Pera, J.; Ros, J.; et al. Lost Writing Uncovered by Laser Two-Photon Fluorescence Provides a Terminus Post Quem for Roman Colonization of Hispania Citerior. *J. Archaeol. Sci.* **2007**, *34* (10), 1594–1600.
- (132) Latour, G.; Echard, J.-P.; Didier, M.; Schanne-Klein, M.-C. In Situ 3d Characterization of Historical Coatings and Wood Using Multimodal Nonlinear Optical Microscopy. *Opt. Express* **2012**, *20* (22), 24623–24623.
- (133) Filippidis, G.; Tserevelakis, G. J.; Selimis, A.; Fotakis, C. Nonlinear Imaging Techniques as Non-Destructive, High-Resolution Diagnostic Tools for Cultural Heritage Studies. *Appl. Phys. A: Mater. Sci. Process.* **2015**, *118* (2), 417–423.
- (134) Masters, B. R.; So, P. T.; Gratton, E. Multiphoton Excitation Fluorescence Microscopy and Spectroscopy of in Vivo Human Skin. *Biophys. J.* **1997**, *72* (6), 2405–12.
- (135) Fukuma, T.; Kimura, M.; Kobayashi, K.; Matsushige, K.; Yamada, H. Development of Low Noise Cantilever Deflection Sensor for Multienvironment Frequency-Modulation Atomic Force Microscopy. *Rev. Sci. Instrum.* **2005**, *76* (5), 053704–8.